Cathodic corrosion

Hersbach, T.J.P.

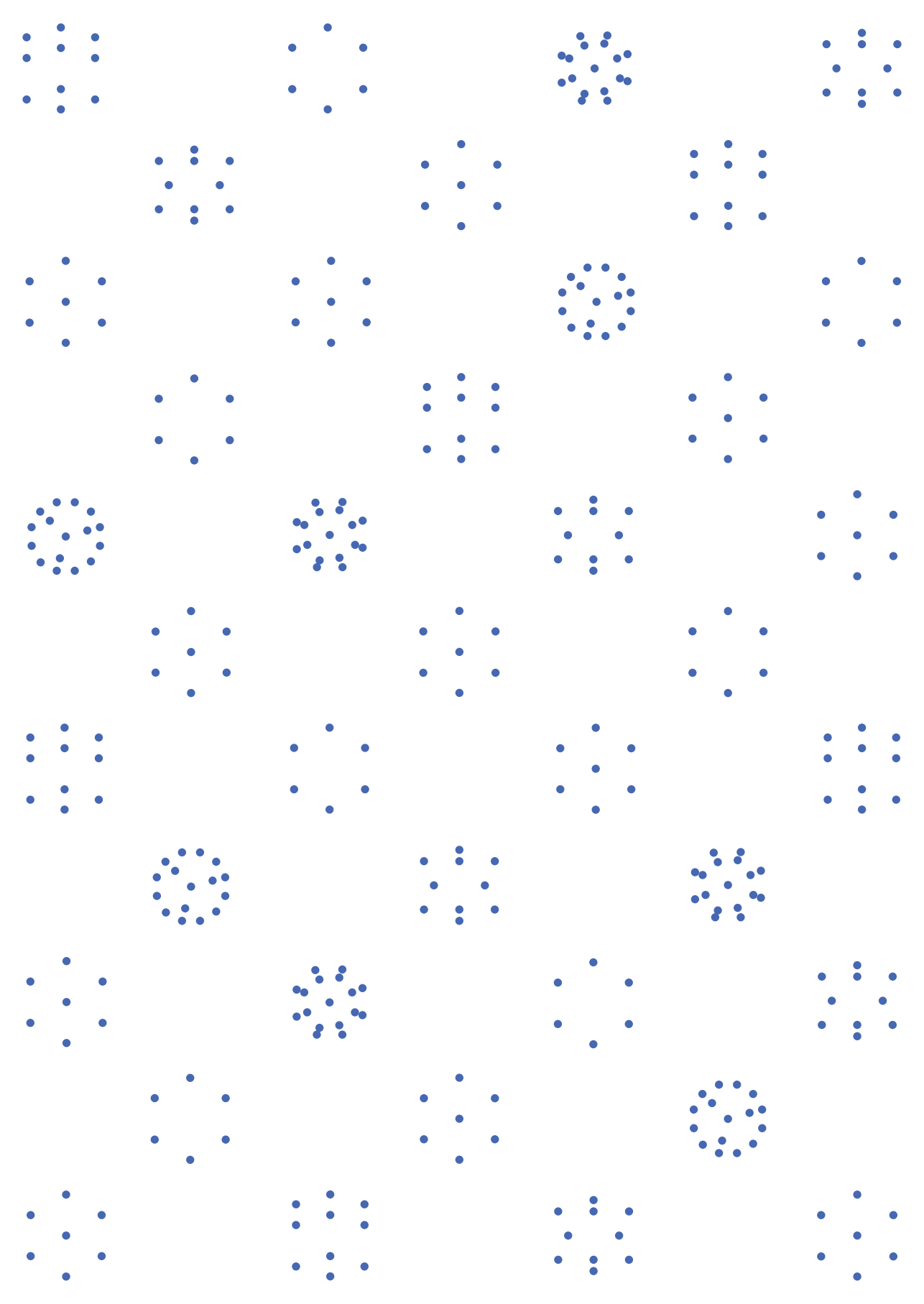

A Supplementary Information for Chapter 4

A.1 Calculated surface structures

This section contains images of the calculated Pt, Rh, and Au structures with adsorbed water (*H_2O), in the absence and presence of adsorbed sodium (*Na) (Fig. A.1–A.3). Additional structures were calculated for adsorbed lithium and potassium. Because these structures are similar to those with adsorbed sodium, their visualizations are omitted for brevity.

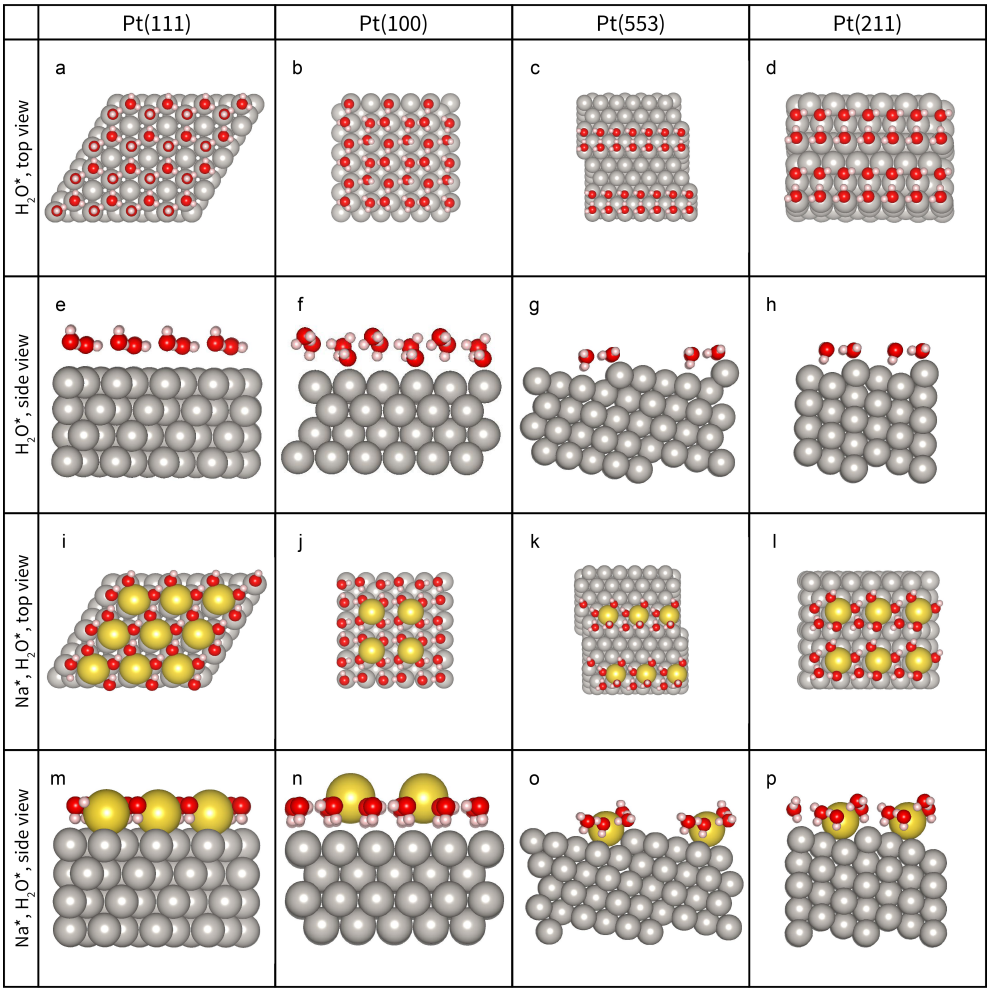

Fig. A.1 | Visualizations of the minimum-energy structures for Pt(111) **(a**, **e**, **i**, **m)**, Pt(100) **(b**, **f**, **j**, **n)**, Pt(553) **(c**, **g**, **k**, **o)** & Pt(211) **(d**, **h**, **l**, **p)**. Adsorbed water (*H_2O) is displayed in red and white, while sodium (*Na) is displayed in yellow.

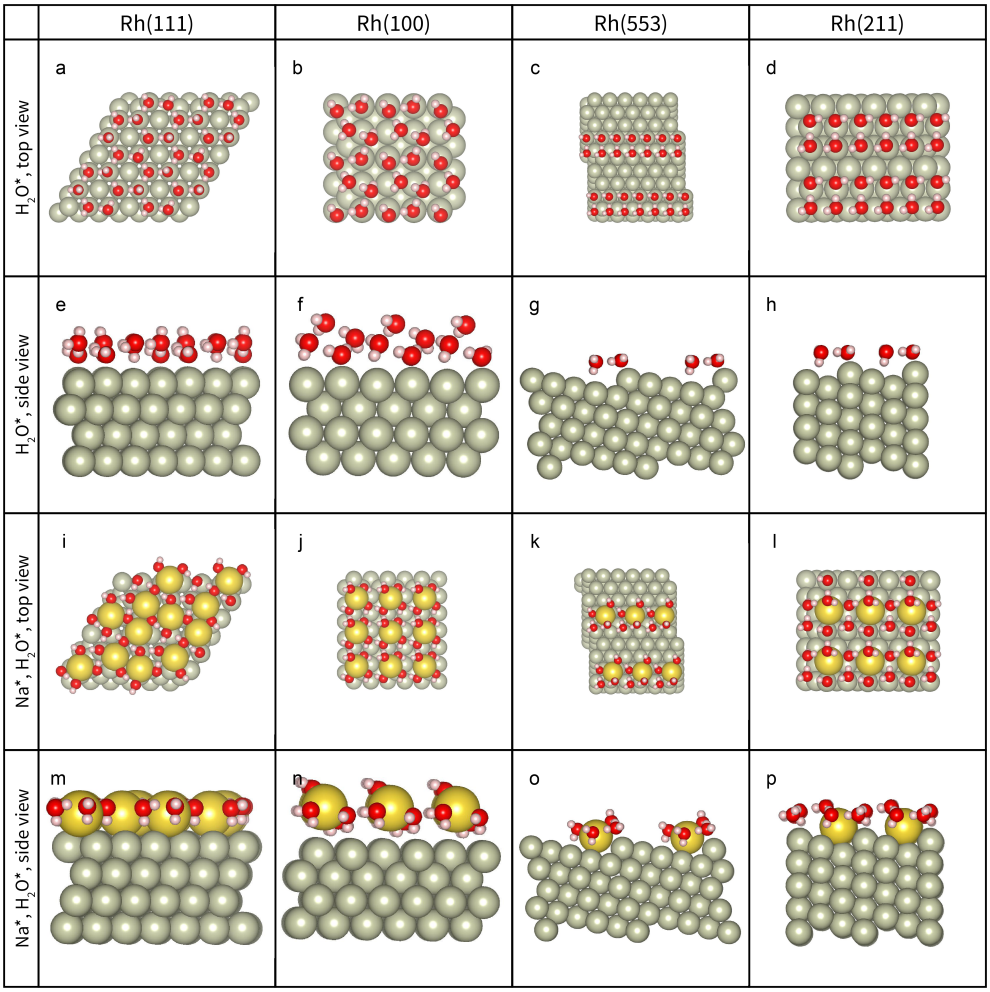

Fig. A.2 | Visualizations of the minimum-energy structures for Rh(111) **(a**, **e**, **i**, **m)**, Rh(100) **(b**, **f**, **j**, **n)**, Rh(553) **(c**, **g**, **k**, **o)** & Rh(211) **(d**, **h**, **l**, **p)**. Adsorbed water (*H_2O) is displayed in red and white, while sodium (*Na) is displayed in yellow.

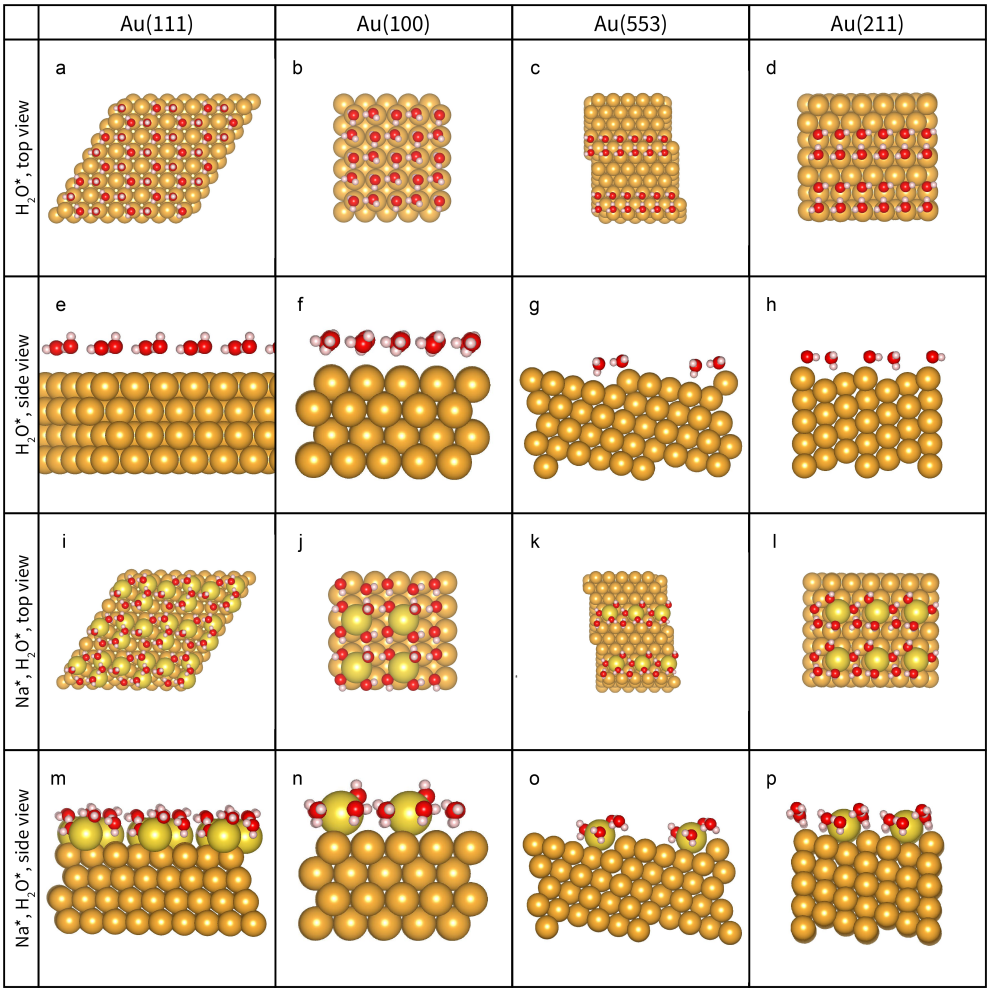

Fig. A.3 | Visualizations of the minimum-energy structures for Au(111) **(a, e, i, m)**, Au(100) **(b, f, j, n)**, Au(553) **(c, g, k, o)** & Au(211) **(d, h, l, p)**. Adsorbed water (*H_2O) is displayed in red and white, while sodium (*Na) is displayed in yellow.

A.2 Cathodic corrosion progression: voltammetry

This section presents cyclic voltammograms (CVs) for all studied metals and electrolytes, following the template used in Chapter 2 & 3. The presented plots provide a more elaborate representation of the corrosion behavior of the studied systems. As such, they allow for the concrete determination of the onset potential of Pt corrosion. The onset potential of Rh can be found from Fig. 4.5, while Fig. A.29 allows for the determination of the onset potential of Au. All figures in the current section (Fig. A.4 through Fig. A.15) contain a CV before the onset potential in Panel **a**, a CV at the onset potential in Panel **b** and CVs featuring more advanced corrosion in Panel **c** and **d**. For Pt and Au, brief additional discussion is included to support specific statements in Chapter 4. All CVs shown here in red are the *fourth* characterization cycle after cathodic polarization.

A.2.1 Platinum voltammograms

The current paragraph will briefly support the statement that an increasing cation concentration causes the formation of increasingly disordered surface sites. Inspection of the CVs in Fig. 4.1 indicates that corrosion in 1 M NaOH leads primarily to the creation of (100) terraces, which are visible in the CV between 0.3 and 0.4 V *vs.* RHE, at the cost of (110) steps. As such, more long-range order terraces are created as less-ordered features such as steps are removed. Similarly, the significant increase in surface area after corrosion in 5 M NaOH is primarily caused by an increase of (100) terrace sites. In contrast, these (100) terrace sites barely increase when corroding in 10 M NaOH. Instead, more steps of both the (100) and (110) orientation are created.

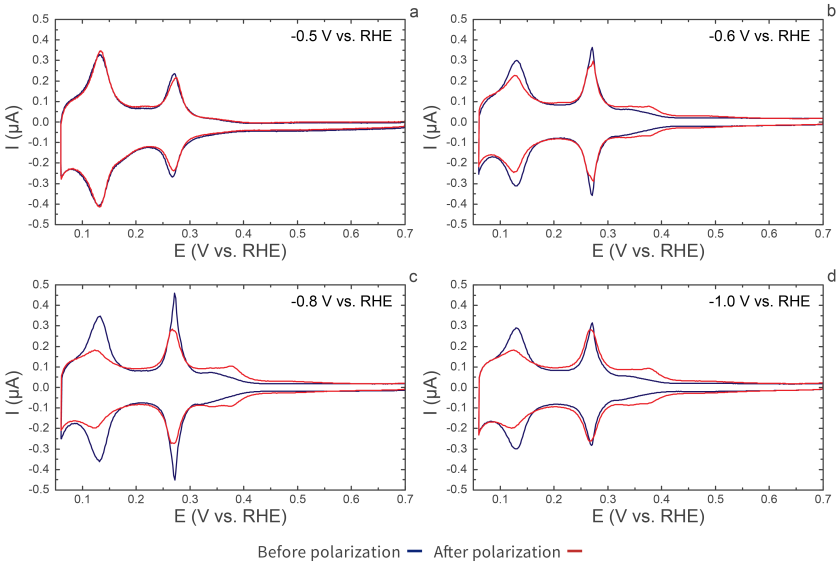

Fig. A.4 | CVs of Pt before (blue trace) and after (red trace) polarization in 1 *M* LiOH at −0.5 *V vs.* RHE **(a)**, −0.6 *V vs.* RHE **(b)**, −0.8 *V vs.* RHE **(c)** and −1.0 *V vs.* RHE **(d)**. CV electrolyte: 0.5 *M* H_2SO_4. Scan rate: 50 $mV \cdot s^{-1}$.

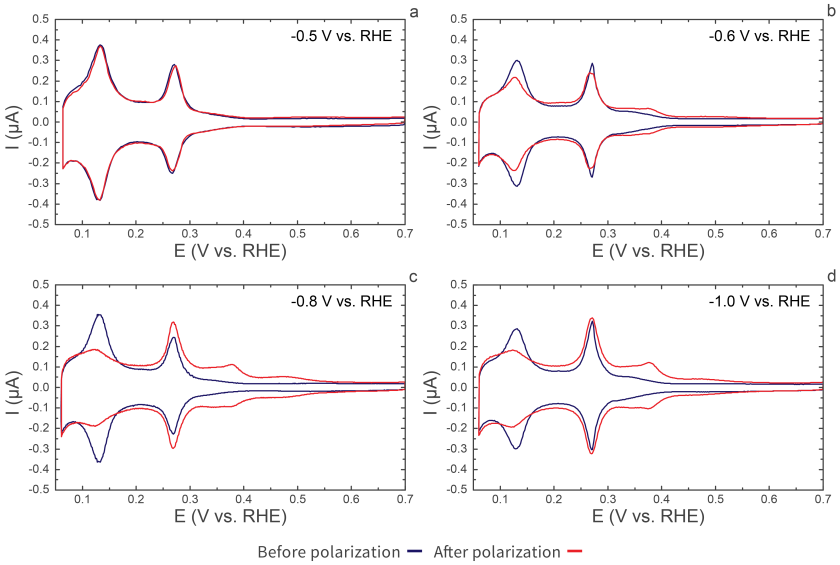

Fig. A.5 | CVs of Pt before (blue trace) and after (red trace) polarization in 1 *M* NaOH at −0.5 *V vs.* RHE **(a)**, −0.6 *V vs.* RHE **(b)**, −0.8 *V vs.* RHE **(c)** and −1.0 *V vs.* RHE **(d)**. CV electrolyte: 0.5 *M* H_2SO_4. Scan rate: 50 $mV \cdot s^{-1}$.

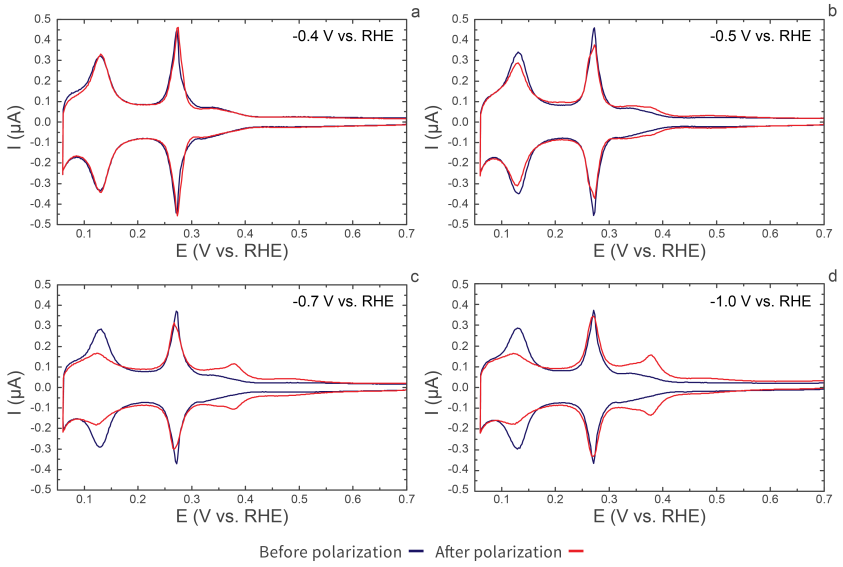

Fig. A.6 | CVs of Pt before (blue trace) and after (red trace) polarization in 1 *M* KOH at −0.4 *V vs.* RHE **(a)**, −0.5 *V vs.* RHE **(b)**, −0.7 *V vs.* RHE **(c)** and −1.0 *V vs.* RHE **(d)**. CV electrolyte: 0.5 *M* H_2SO_4. Scan rate: 50 $mV \cdot s^{-1}$.

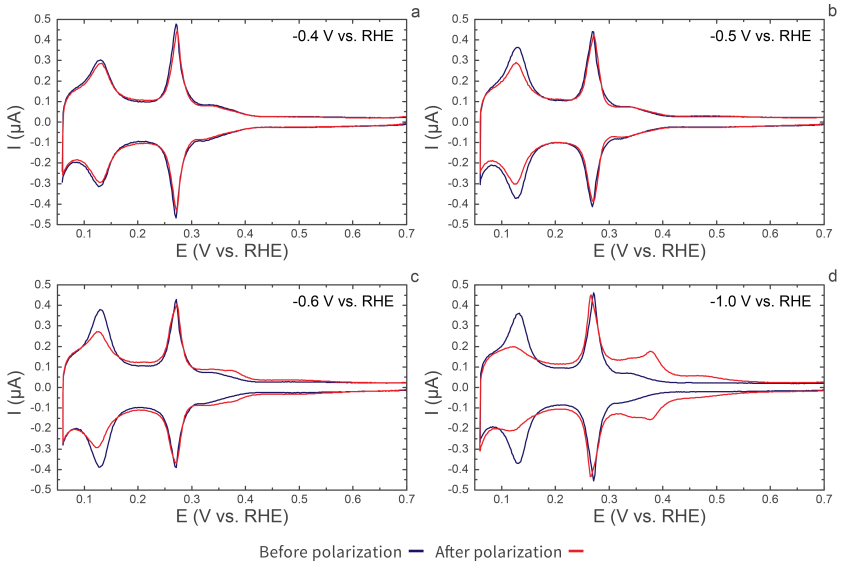

Fig. A.7 | CVs of Pt before (blue trace) and after (red trace) polarization in 5 *M* LiOH at −0.4 *V vs.* RHE **(a)**, −0.5 *V vs.* RHE **(b)**, −0.6 *V vs.* RHE **(c)** and −1.0 *V vs.* RHE **(d)**. CV electrolyte: 0.5 *M* H_2SO_4. Scan rate: 50 $mV \cdot s^{-1}$.

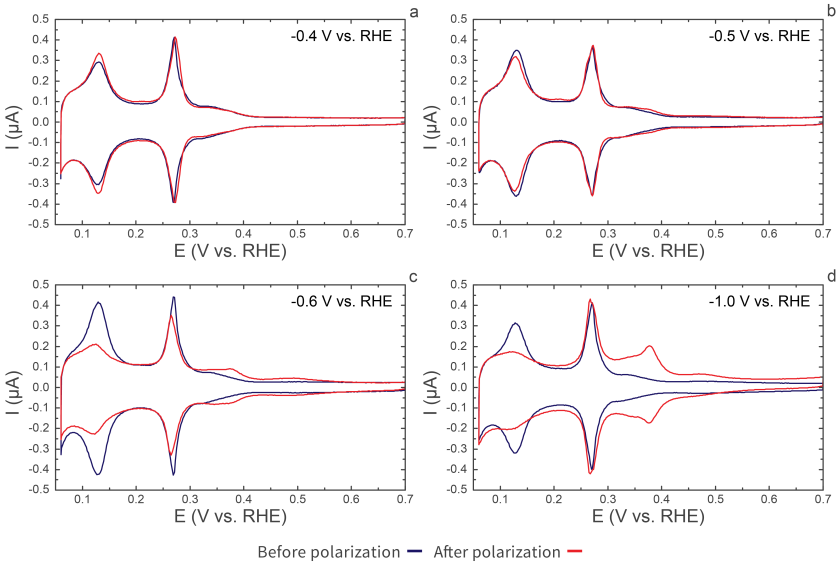

Fig. A.8 | CVs of Pt before (blue trace) and after (red trace) polarization in 5 *M* NaOH at −0.4 *V vs.* RHE **(a)**, −0.5 *V vs.* RHE **(b)**, −0.6 *V vs.* RHE **(c)** and −1.0 *V vs.* RHE **(d)**. CV electrolyte: 0.5 *M* H_2SO_4. Scan rate: 50 $mV \cdot s^{-1}$.

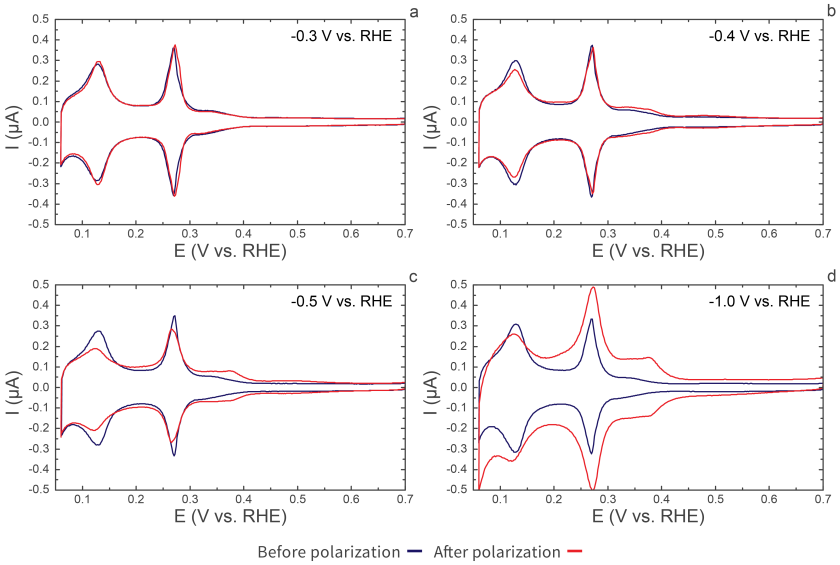

Fig. A.9 | CVs of Pt before (blue trace) and after (red trace) polarization in 5 *M* KOH at −0.3 *V vs.* RHE **(a)**, −0.4 *V vs.* RHE **(b)**, −0.5 *V vs.* RHE **(c)** and −1.0 *V vs.* RHE **(d)**. CV electrolyte: 0.5 *M* H_2SO_4. Scan rate: 50 $mV \cdot s^{-1}$.

A.2.2 Rhodium voltammograms

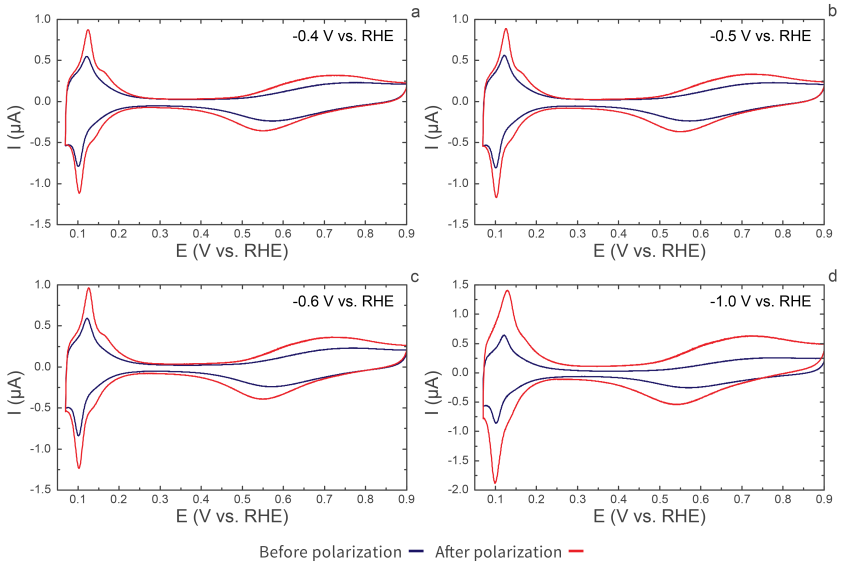

Fig. A.10 | CVs of Rh before (blue trace) and after (red trace) polarization in 5 *M* LiOH at −0.4 *V vs.* RHE **(a)**, −0.5 *V vs.* RHE **(b)**, −0.6 *V vs.* RHE **(c)** and −1.0 *V vs.* RHE **(d)**. CV electrolyte: 0.1 *M* H_2SO_4. Scan rate: 50 $mV \cdot s^{-1}$.

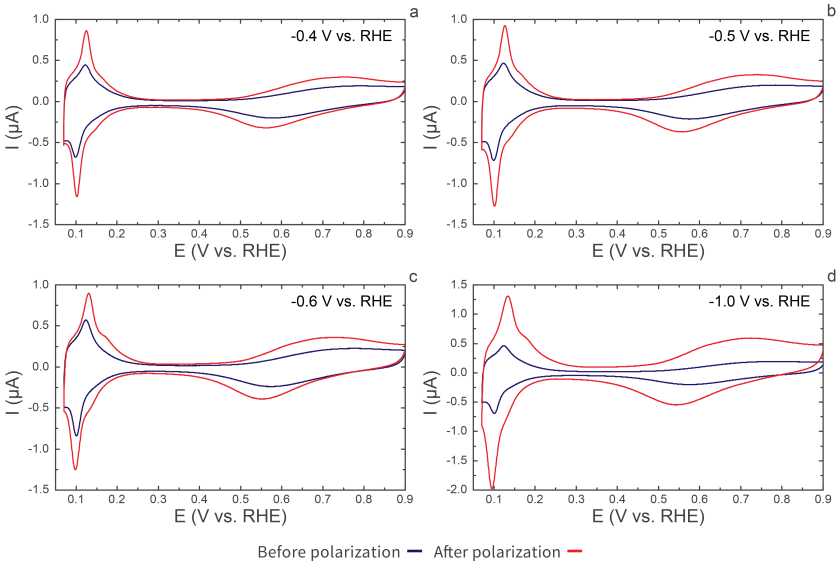

Fig. A.11 | CVs of Rh before (blue trace) and after (red trace) polarization in 5 *M* NaOH at −0.4 *V vs.* RHE **(a)**, −0.5 *V vs.* RHE **(b)**, −0.6 *V vs.* RHE **(c)** and −1.0 *V vs.* RHE **(d)**. CV electrolyte: 0.1 *M* H_2SO_4. Scan rate: 50 $mV \cdot s^{-1}$.

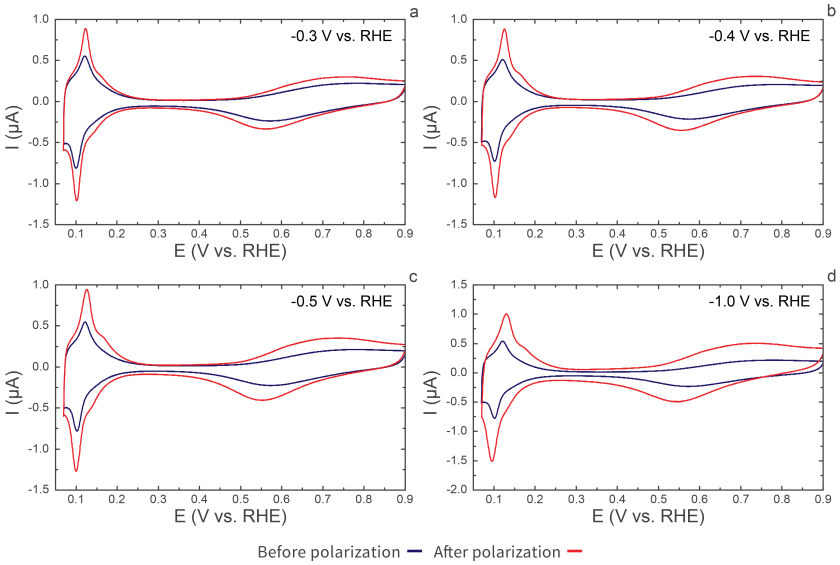

Fig. A.12 | CVs of Rh before (blue trace) and after (red trace) polarization in 5 *M* KOH at −0.3 *V vs.* RHE **(a)**, −0.4 *V vs.* RHE **(b)**, −0.5 *V vs.* RHE **(c)** and −1.0 *V vs.* RHE **(d)**. CV electrolyte: 0.1 *M* H_2SO_4. Scan rate: 50 $mV \cdot s^{-1}$.

A.2.3 Gold voltammograms

The present section will briefly elaborate on the shape of Au voltammograms that are shown here and in Chapter 4. As indicated in Fig. 4.7 and Fig. A.13, corrosion in LiOH induces only small changes in the cyclic voltammogram of Au, whereas more pronounced changes are found for corrosion in NaOH. Beside the differences addressed in Chapter 4, the Au voltammograms after NaOH corrosion (Fig. A.14) also exhibit a pair of peaks at 1.38 and 1.42 V *vs.* RHE. These peaks are sharp and positioned at slightly higher and lower potentials, respectively, compared to the (100) peak on electrodes corroded in LiOH. Thus, the pair of peaks likely corresponds to a small amount of (100) and (111) step sites, of which the CV signal is superimposed on the (100) terrace peak. The presence of this peak pair and of the sharp (111) peak suggest a pronounced difference in corrosion behavior with respect to LiOH.

A similarly pronounced difference is found for corrosion in 5 M KOH (Fig. 4.7 & Fig. A.15), which shows a remarkable evolution between the first and fourth CV cycle after corrosion. Though the reason for this evolution is unknown, it does match the dramatic change in facet distribution between the first and fourth cycle. During the first cycle, the electrode appears rather amorphous, resembling a freshly polished electrode that has perhaps undergone several cycles of voltammetry;[1] a sharp peak corresponding to (100) sites is virtually absent in the voltammogram. The shape of this voltammogram changes readily after undergoing several additional cycles to yield an electrode that resembles a sample corroded in 5 M LiOH, but with slightly more step sites, (110) terrace sites and (111) sites.

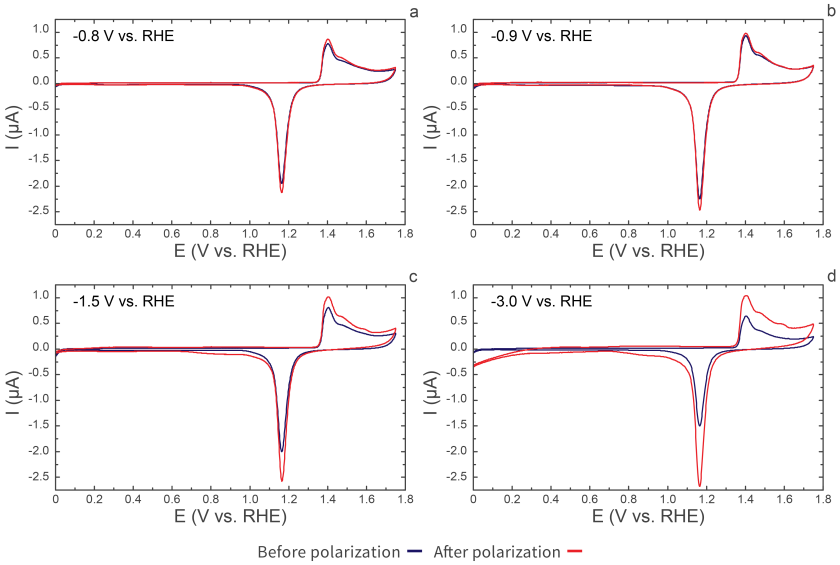

Fig. A.13 | CVs of Au before (blue trace) and after (red trace) polarization in 5 *M* LiOH at −0.8 *V vs.* RHE **(a)**, −0.9 *V vs.* RHE **(b)**, −1.5 *V vs.* RHE **(c)** and −3.0 *V vs.* RHE **(d)**. CV electrolyte: 0.1 *M* H_2SO_4. Scan rate: 50 $mV \cdot s^{-1}$.

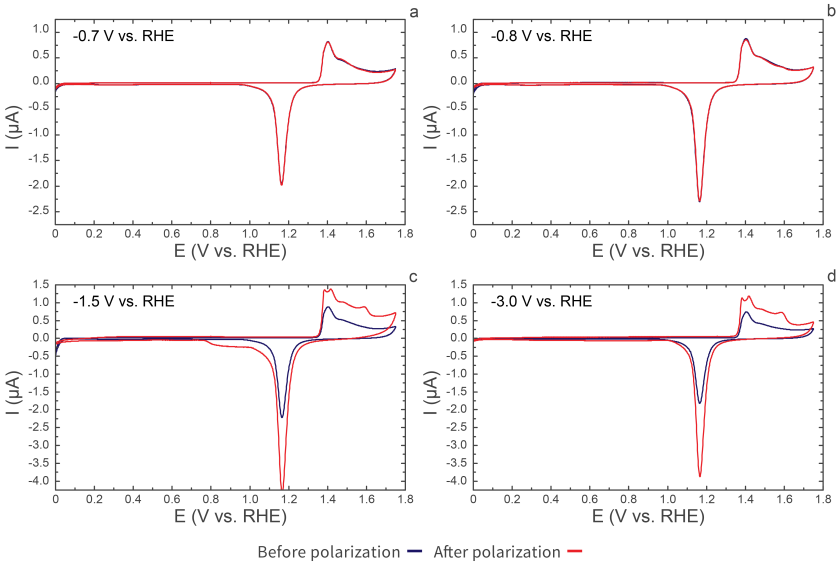

Fig. A.14 | CVs of Au before (blue trace) and after (red trace) polarization in 5 *M* NaOH at −0.7 *V vs.* RHE **(a)**, −0.8 *V vs.* RHE **(b)**, −1.5 *V vs.* RHE **(c)** and −3.0 *V vs.* RHE **(d)**. CV electrolyte: 0.1 *M* H_2SO_4. Scan rate: 50 $mV \cdot s^{-1}$.

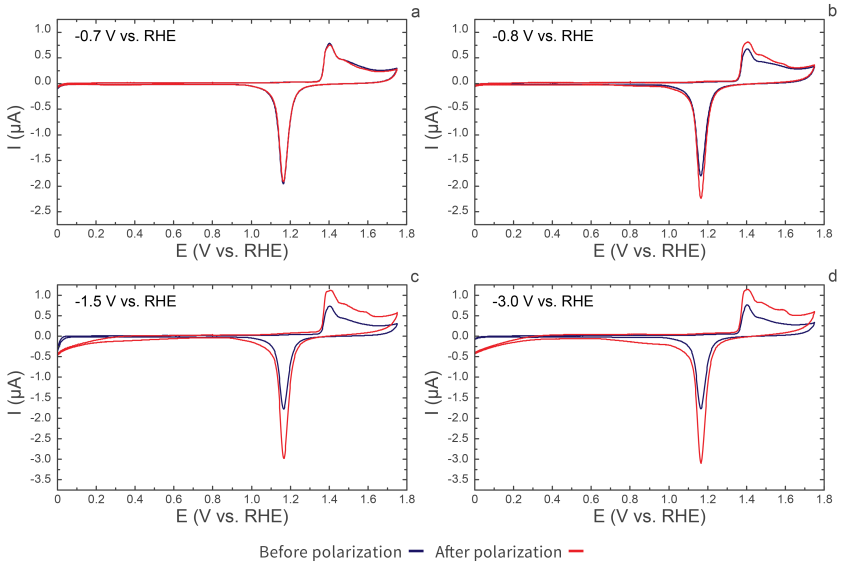

Fig. A.15 | CVs of Au before (blue trace) and after (red trace) polarization in 5 *M* KOH at −0.7 *V vs.* RHE **(a)**, −0.8 *V vs.* RHE **(b)**, −1.5 *V vs.* RHE **(c)** and −3.0 *V vs.* RHE **(d)**. CV electrolyte: 0.1 *M* H_2SO_4. Scan rate: 50 $mV \cdot s^{-1}$.

A.3 Cathodic corrosion progression: scanning electron microscopy

This section displays scanning electron micrographs that illustrate the progression of cathodic corrosion as function of the applied electrode potential. These figures are arranged in the same order as the figures in the previous section. Though most figures can be interpreted readily with the information provided in Chapter 4, several electrode features that are not caused by cathodic corrosion are highlighted here for clarity:

- On Pt electrodes, some facets contain roughness that is visible as lines in the micrographs, as can be seen in Fig. A.16 **d**, **e**, Fig. A.18 **b**, **d**, Fig. A.19 **a**, **d**, Fig. A.20 **a**, **d** and Fig. A.21 **d**. These features were also observed for electrodes that were polarized at less cathodic potentials than the onset of cathodic corrosion and are therefore likely not signs of cathodic corrosion.

- On Rh electrodes, which were not annealed in this study, cracks, pits and ridges such as those in Panel **a** of Fig. A.22 through Fig. A.24 are present. These cracks are also visible on unpolarized electrodes and are therefore not considered signs of

cathodic corrosion (Chapter 3).

- On Au, cracks similar to those observed on rhodium are present. These are similarly observed on untreated electrodes and therefore not thought to be features of cathodic corrosion.

Beside these remarks, several paragraphs of additional discussion are included below for each metal.

A.3.1 Platinum micrographs

This paragraph will briefly illustrate cathodic corrosion in 1 M electrolytes and motivate the statement that the extent of cathodic corrosion increases with cation size. Starting with LiOH (Fig. A.16), no pronounced roughening is visible at -1.0 V *vs.* RHE, but triangular etch pits can be observed at more negative potentials. More significant roughening is visible for NaOH (Fig. A.17), which induces the formation of triangular etch pits at less negative potentials than in 1 M LiOH. At more negative potentials, this more extensive corrosion causes the formation of nanoscale corrugation in NaOH. KOH (Fig. A.18) completes this trend, with electrodes appearing slightly more corrugated than in NaOH.

Along with corrosion depending on the cation, it is also sensitive to the applied potential. Interestingly, this dependence appears similar in SEM after corrosion at mild potentials. Specifically, SEM indicates that corrosion starts at triangular (100) etch pits. This is illustrated by electrodes corroded in 5 M NaOH, which contain triangular features within some regions where more severe corrosion occurs (Fig. 4.4 **e** & Fig. A.20 **f**). These features bear resemblance to the well-defined triangular etch pits observed at less negative potentials (Fig. A.20 **b**). It is therefore possible that such well-defined pits serve as starting points of cathodic corrosion: severe corrosion could cause the sides of a triangle to extend into the features in Fig. 4.4 **e**. Selective extension of one triangle side due to curvature of the electrode might even lead to the formation of the etch lines in Fig. 4.2 **b** and Fig. 4.4 **b**. Similar arguments can be based on the corrosion behavior in 1 M NaOH and KOH (Fig. A.17–A.18).

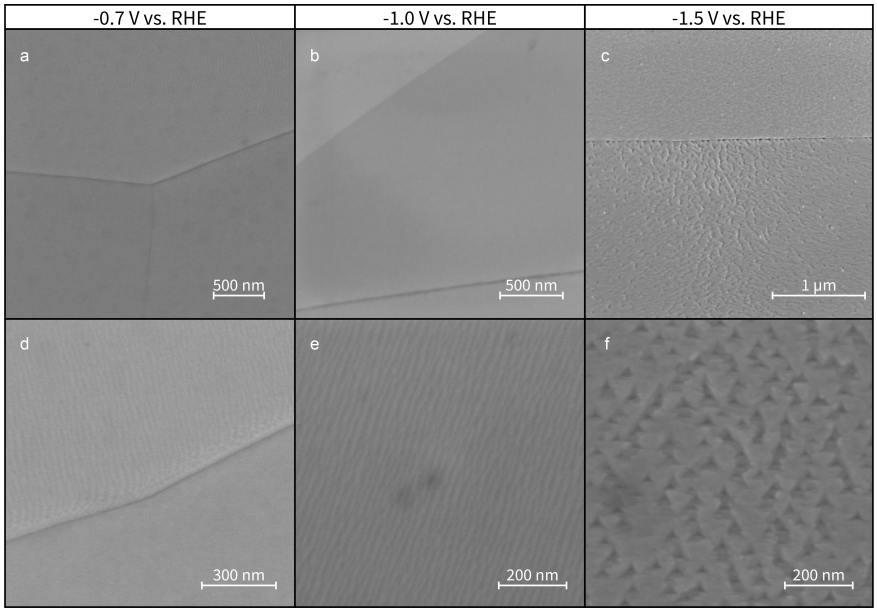

Fig. A.16 | Scanning electron micrographs of Pt electrodes corroded at 1 *M* LiOH at −0.7 *V vs.* RHE **(a**, **d)**, −1.0 *V vs.* RHE **(b**, **e)** and −1.5 *V vs.* RHE **(c**, **f)**.

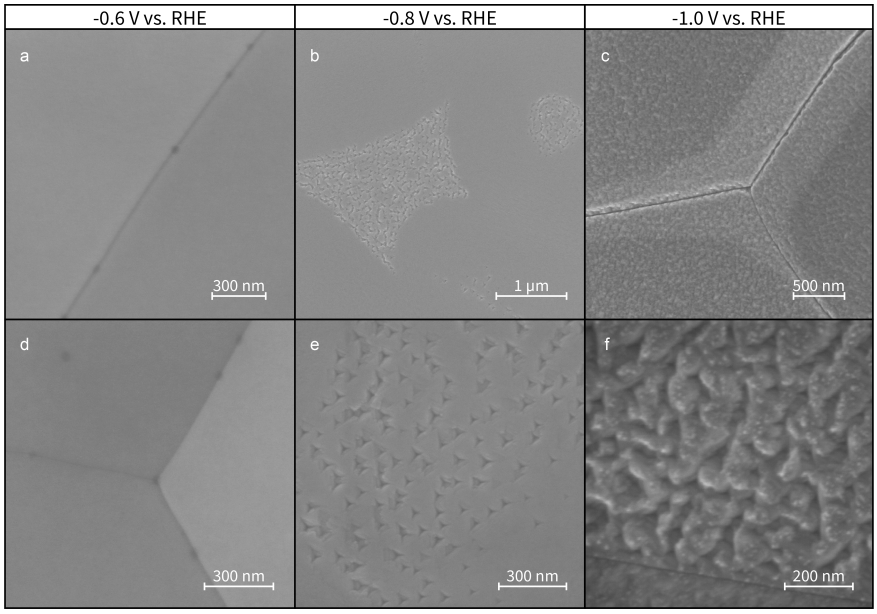

Fig. A.17 | Scanning electron micrographs of Pt electrodes corroded at 1 *M* NaOH at −0.6 *V vs.* RHE **(a**, **d)**, −0.8 *V vs.* RHE **(b**, **e)** and −1.0 *V vs.* RHE **(c**, **f)**.

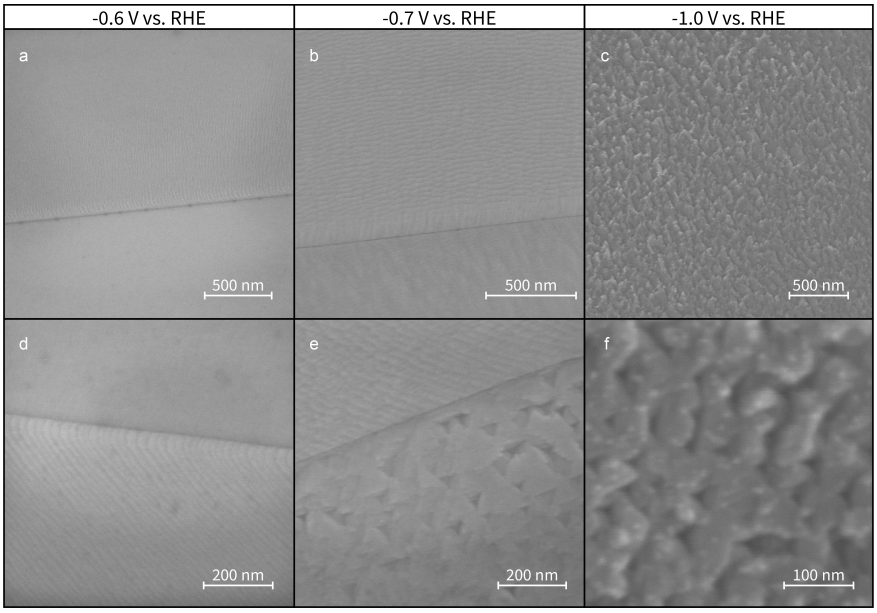

Fig. A.18 | Scanning electron micrographs of Pt electrodes corroded at 1 *M* KOH at −0.6 *V vs.* RHE **(a**, **d)**, −0.7 *V vs.* RHE **(b**, **e)** and −1.0 *V vs.* RHE **(c**, **f)**.

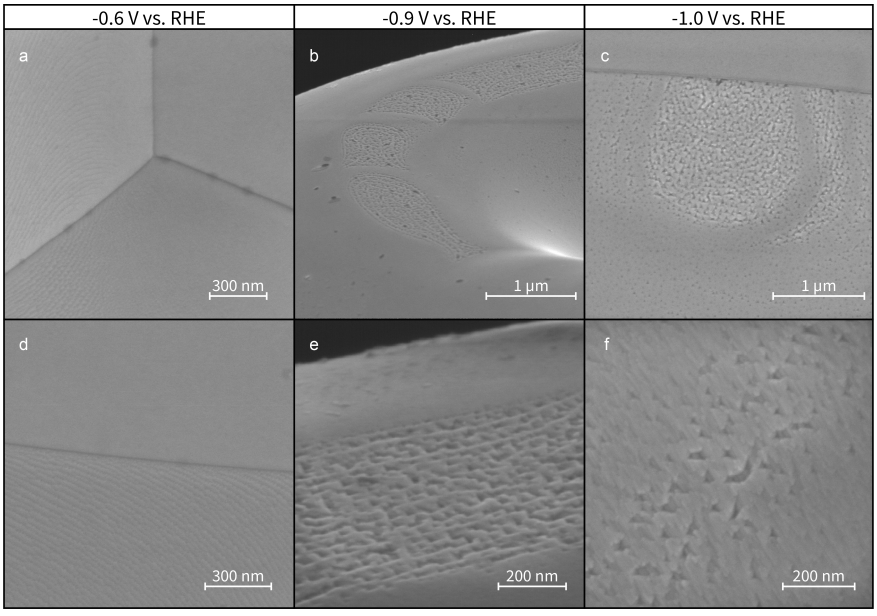

Fig. A.19 | Scanning electron micrographs of Pt electrodes corroded at 5 *M* LiOH at −0.6 *V vs.* RHE **(a**, **d)**, −0.9 *V vs.* RHE **(b**, **e)** and −1.0 *V vs.* RHE **(c**, **f)**.

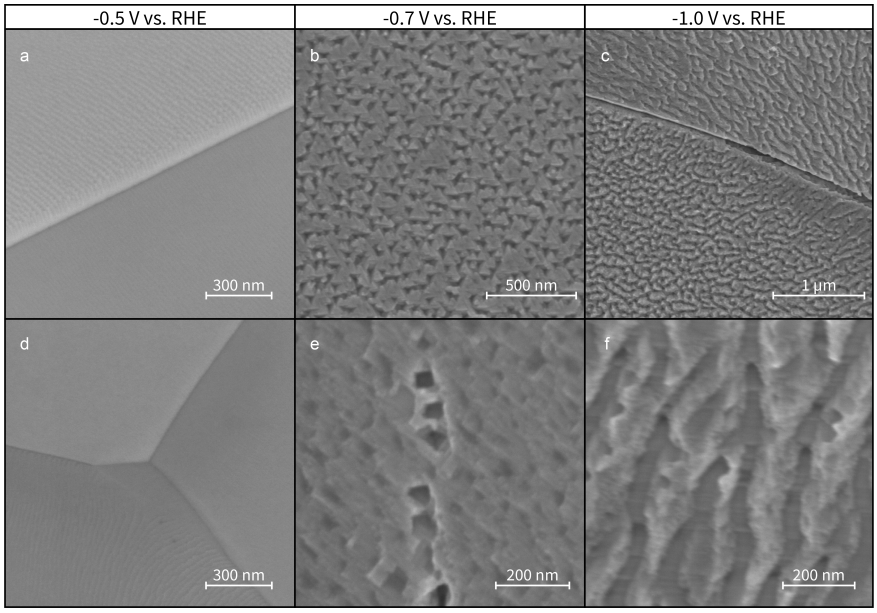

Fig. A.20 | Scanning electron micrographs of Pt electrodes corroded at *5 M* NaOH at −0.5 *V vs.* RHE **(a**, **d)**, −0.7 *V vs.* RHE **(b**, **e)** and −1.0 *V vs.* RHE **(c**, **f)**.

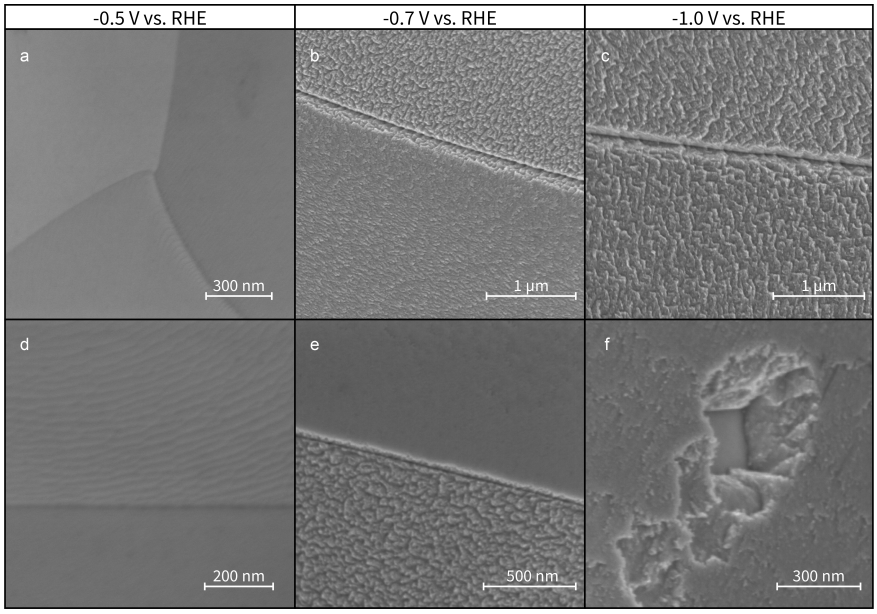

Fig. A.21 | Scanning electron micrographs of Pt electrodes corroded at *5 M* KOH at −0.5 *V vs.* RHE **(a**, **d)**, −0.7 *V vs.* RHE **(b**, **e)** and −1.0 *V vs.* RHE **(c**, **f)**.

A.3.2 Rhodium micrographs

The current three paragraphs will briefly elaborate on the discussion of the Rh scanning electron micrographs in Chapter 4. As mentioned in this chapter, Rh appears mainly uncorroded after corrosion in 5 *M* LiOH. One exception to this statement is a single electrode that was treated at −1.0 *V vs.* RHE. This electrode, which was one of three electrodes that was corroded at this potential and subsequently imaged, contained etching features close to where the electrode was cut from the spool (Fig. A.22 **c**). These etching features resemble those found after treatment in 10 *M* NaOH and therefore likely correspond to the formation of (100) sites.

More severe corrosion is found for Rh, corroded in 5 *M* NaOH. After corrosion at −0.8 *V vs.* RHE, small particles can mainly be found in areas close to where the wire was cut. In contrast, significantly more particles and even etch pits are widespread at −0.9 and −1.0 *V vs.* RHE. The etch pits are several hundreds of nanometers wide and can be up to several micrometers long. They are therefore the largest Rh etch pits found in this study.

Smaller features are found after corrosion in 5 *M* KOH, in which many small particles are created. These particles are occasionally oriented around a small central etch pit (Fig. 4.6 **c**); such pits are either the source of the particles or instead caused most particles to be displaced around it to form a halo-like arrangement. In any case, a high coverage of particles was observed for all three electrodes imaged after polarization at −1.0 *V vs.* RHE in 5 *M* KOH.

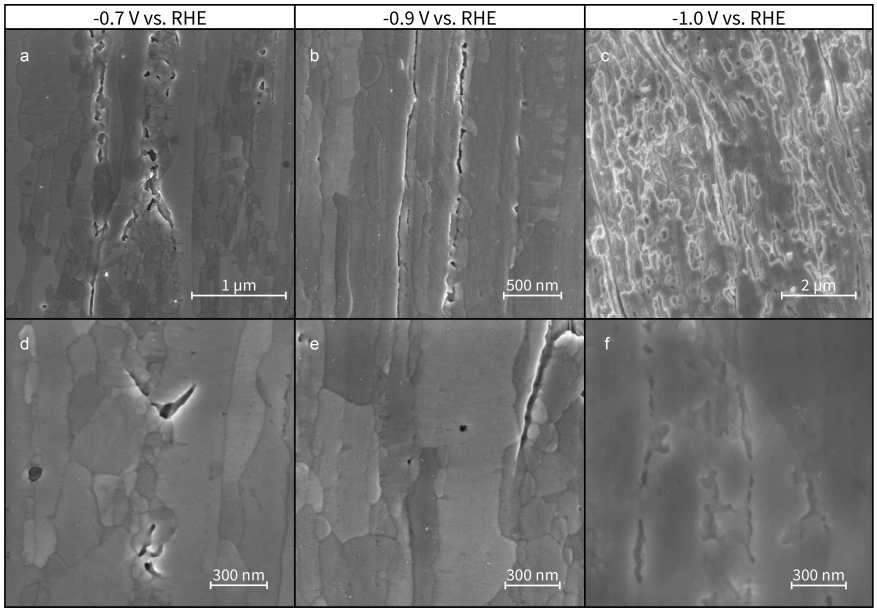

Fig. A.22 | Scanning electron micrographs of Rh electrodes corroded at *5 M* LiOH at *−0.7 V vs.* RHE **(a, d)**, *−0.9 V vs.* RHE **(b, e)** and *−1.0 V vs.* RHE **(c, f)**.

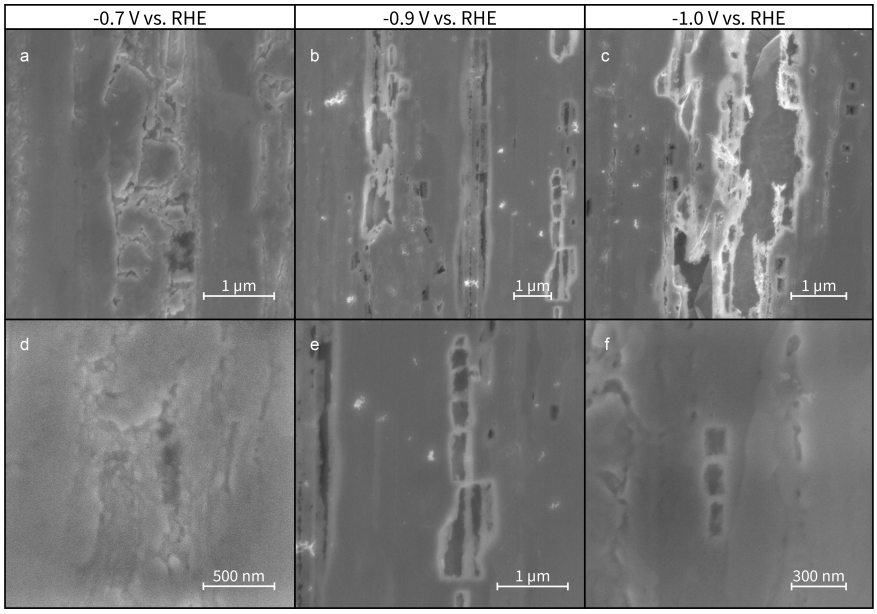

Fig. A.23 | Scanning electron micrographs of Rh electrodes corroded at *5 M* NaOH at *−0.7 V vs.* RHE **(a, d)**, *−0.9 V vs.* RHE **(b, e)** and *−1.0 V vs.* RHE **(c, f)**.

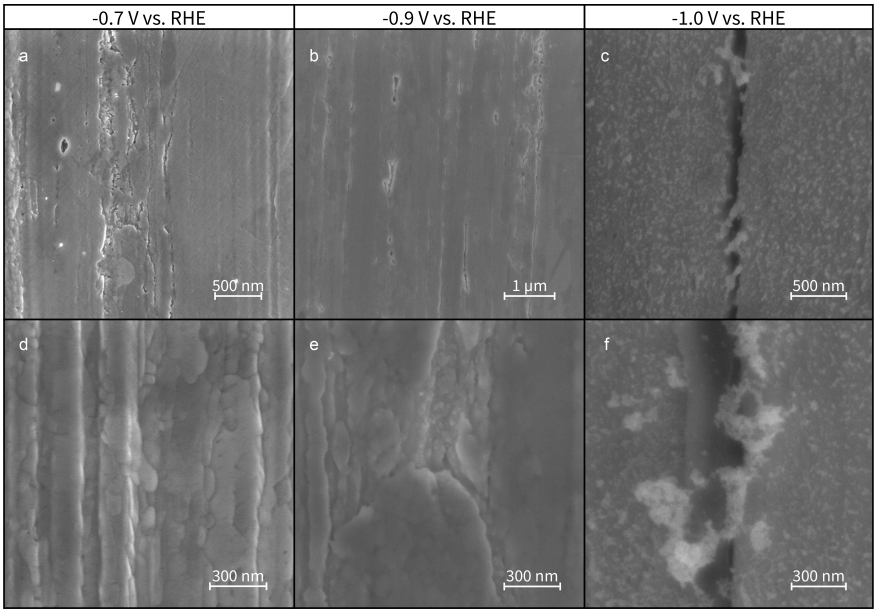

Fig. A.24 | Scanning electron micrographs of Rh electrodes corroded at *5 M* KOH at −0.7 *V vs.* RHE **(a**, **d)**, −0.9 *V vs.* RHE **(b**, **e)** and −1.0 *V vs.* RHE **(c**, **f)**.

A.3.3 Gold micrographs

This paragraph briefly describes the (100)-oriented etch pits on gold after corrosion in *5 M* LiOH. The rectangular pits in Fig. 4.8 **d** with 90-degree outlines and pit walls that descend straight into the surface are similar to those observed for platinum and can be taken as signs of (100)-type pits in a (100) surface (Chapter 2). It should be mentioned that these rectangular (100)-type pits and their triangular counterparts in Fig. A.25 **c** were observed on one electrode in an exploratory study for the current work and on only one of the three electrodes that were imaged after corrosion at -3.0 *V vs.* RHE. The other two electrodes contained more disordered pits, which might be due to these electrode tips having different amounts of stress due to the slightly different cut of the wires. However, all three electrodes exhibited very similar voltammetric profiles. The (100)-type pits therefore seem to be appropriate illustrative examples of the electrochemically detected formation of (100) sites.

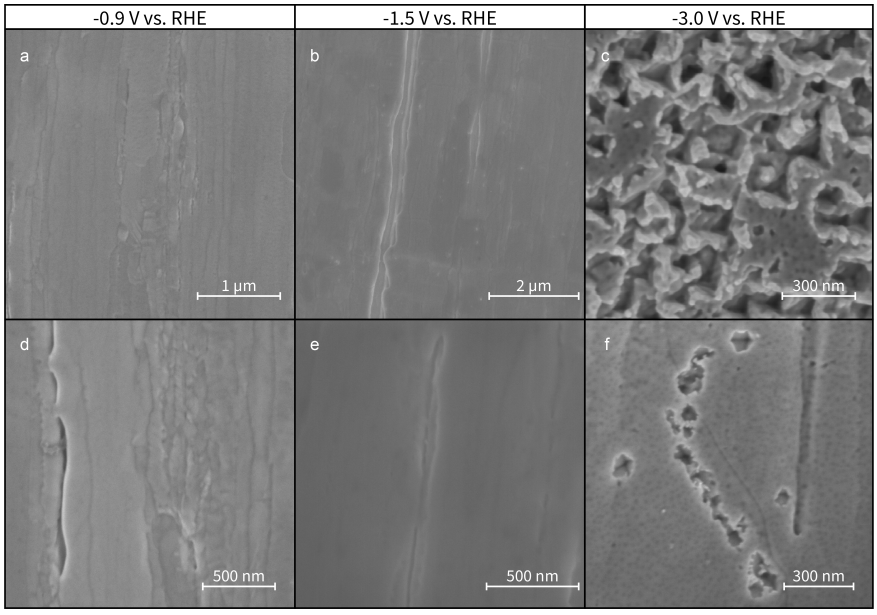

Fig. A.25 | Scanning electron micrographs of Au electrodes corroded at *5 M* LiOH at -0.9 *V vs.* RHE **(a**, **d)**, -1.5 *V vs.* RHE **(b**, **e)** and -3.0 *V vs.* RHE **(c**, **f)**.

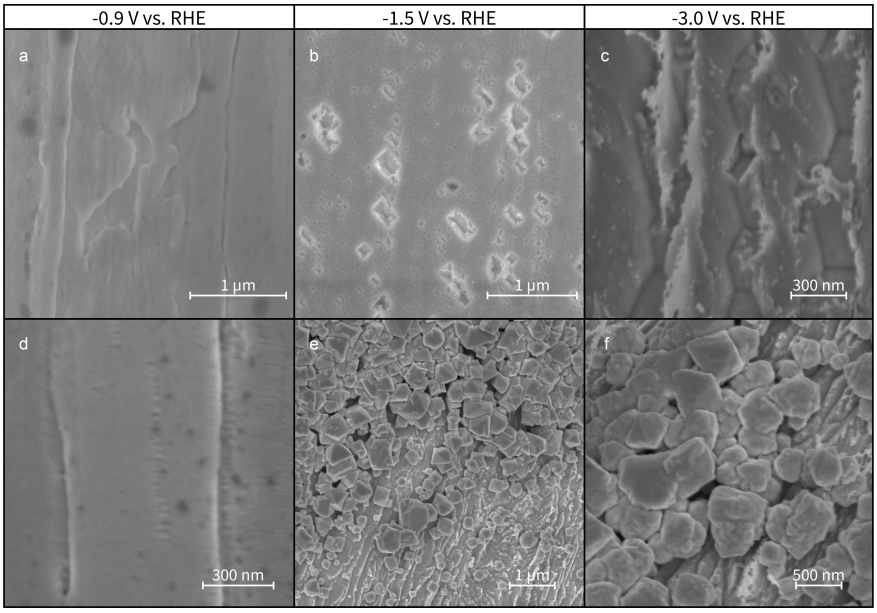

Fig. A.26 | Scanning electron micrographs of Pt electrodes corroded at *5 M* NaOH at −0.9 *V vs.* RHE **(a**, **d)**, −1.5 *V vs.* RHE **(b**, **e)** and −3.0 *V vs.* RHE **(c**, **f)**.

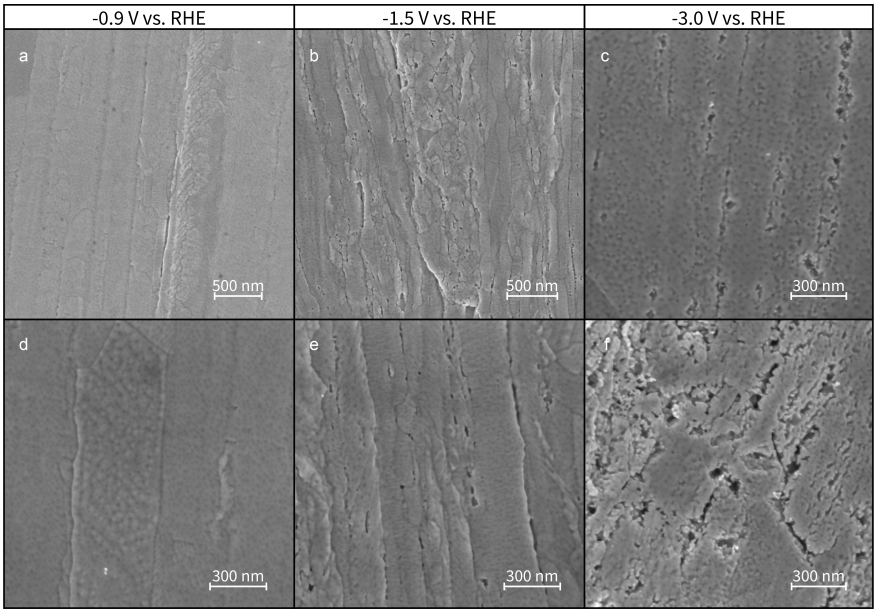

Fig. A.27 | Scanning electron micrographs of Pt electrodes corroded at *5 M* KOH at −0.9 *V vs.* RHE **(a**, **d)**, −1.5 *V vs.* RHE **(b**, **e)** and −3.0 *V vs.* RHE **(c**, **f)**.

A.4 The role of cations at different potentials

The presented data in Chapter 4 and in Fig. A.4–A.27 indicate that cations only weakly influence the final surface structure at mild corrosion potentials. In contrast, the influence of cations is much stronger at more negative corrosion potentials. This might be explained by the cation coverage as a function of potential: though Fig. 4.9 indicates cation adsorption during cathodic corrosion, one can reasonably expect the cation coverage to increase as the potential decreases. At these higher coverages, repulsion between cations can amplify differences between the various cations, compared to less negative potentials. At more negative potentials and higher cation coverages, the cations could therefore modulate the facet preference induced by hydrogen, causing more extensive corrosion (visible in Fig. A.16–A.27) and diverging behavior between electrolytes. This hypothesis would explain the experimental data with theoretically established cation adsorption behavior, and could therefore serve as an appropriate mechanistic hypothesis for further studies of electrolyte effects in cathodic corrosion.

A.5 Model etch pits

This section features three model etch pits, to illustrate how specific features in the scanning electron micrographs correspond to facet distributions seen in cyclic voltammetry. These model pits are displayed in Fig. A.28. The pits are situated in either (111) or (100) surfaces and exclusively have (111) and (100) facets on their pit walls. Pit **a** and **b** match those in Chapter 2, with the exception that the pits shown in the current section do not contain a step edge. For a more elaborate explanation of these etch pits, the reader is referred to Chapter 2 & 3.

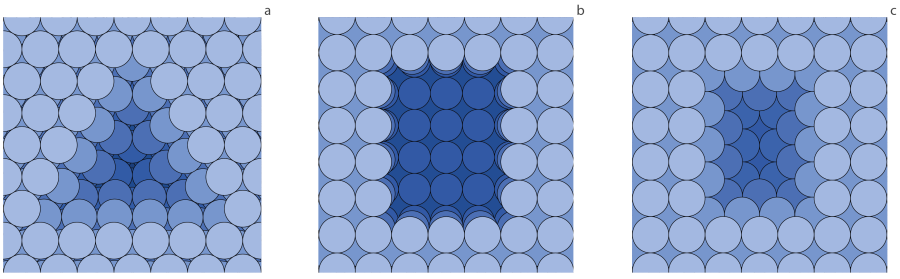

Fig. A.28 | Three model etch pits: a pit with (100)-oriented walls in a (111) surface **(a)**, a pit with (100)-oriented walls in a (100) surface **(b)** and a pit with (111)-oriented walls in a (100) surface **(c)**.

A.6 Gold onset potential determination

As for gold corrosion in 10 M NaOH (Chapter 3), the first sign of cathodic corrosion is the appearance of a peak corresponding to (111) sites around 1.58 V *vs.* RHE. The formation of these (111) sites is therefore used to determine the corrosion onset potential in 5 M LiOH, 5 M NaOH and 5 M KOH. This is done by comparing cyclic voltammograms of Au electrodes, polarized around the onset potential, presented in Panel **a**, **c** and **e** of Fig. A.29. In these CVs, the currents are converted to current densities by calculating the electrode surface area through the oxide reduction peak. To do so, the charge of the peak was calculated by integrating it. It was then used to calculate the surface area, by using a specific charge of 390 $\mu A \cdot cm^{-2}$.[2] In order to emphasize the formation of the (111) peak, the derivatives of the current density traces are also presented in Panel **b**, **d** & **f**.

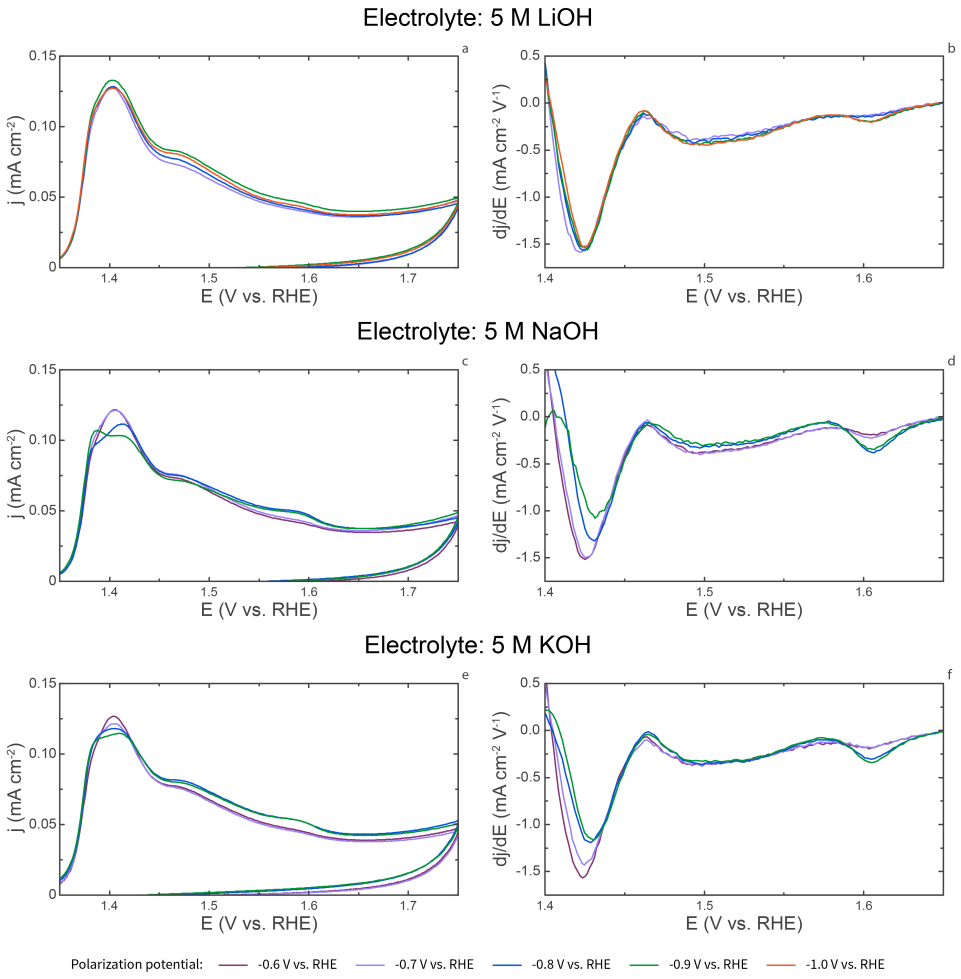

Fig. A.29 | Normalized cyclic voltammograms **(a, c, e)** and derivatives of the voltammograms **(b, d, f)** of Au electrodes polarized around the corrosion onset potential in 5 M LiOH **(a, b)**, 5 M NaOH **(c, d)** and 5 M KOH **(e, f)**. CV electrolyte: 0.1 M H_2SO_4. Scan rate: 50 $mV \cdot s^{-1}$.

A.7 Computational cation adsorption in vacuum

In addition to calculating cation adsorption while explicitly considering solvation, we also performed calculations for cation adsorption in vacuum. These calculations can directly be compared to those in Chapter 3, which also includes details on the employed computational procedure. The calculated adsorption energies are displayed in Fig. A.30 and indicate that the adsorption of Li is stronger on all of the surfaces than Na or K. This matches the trend we find in Chapter 4 at high cation coverage when including near-surface solvation. As such, the trend in Fig. A.30 is exactly opposite from that found for lower coverage. This indicates that, at lower coverage, solvation may play a significant role in stabilizing the adsorption of the larger cations. The stronger stabilization of these larger cations is supported by the fact that the larger cations retain more of their charge upon adsorption, which would induce more repulsion between neighboring cations and thus a larger interaction with the solvent.

An additional difference between the results in Fig. A.30 and those in Chapter 4 is the calculated facet preference. Though both results generally agree in adsorption being strongest on (100) facets and steps for platinum, the results in Fig. A.30 also suggest this to be the case for the adsorption of Li and Na on Rh, as well as for Li adsorption on Au. In fact, closer examination of the numbers in Fig. A.30 indicates that the preference for adsorption on (100) steps forms a monotonic trend as a function of cation size (Fig. A.31), with Li exhibiting the strongest preference for (211) over (553), followed by Na and K. This trend is not present on the Rh and Au surfaces in the presence of near-surface solvation in Chapter 4, which can be explained in two ways:

- Solvation promotes adsorption in such a way that the binding strength is less dependent on surface structure on Rh and Au than it is on Pt.
- Different solvation structures must be investigated on the Rh and Au surfaces in order to capture solvation more accurately.

For these two reasons, future work should examine the sensitivity of the calculated trends in adsorption to the degree of explicit solvation. In addition, this work should probe the role of the particular water structure examined on each surface.

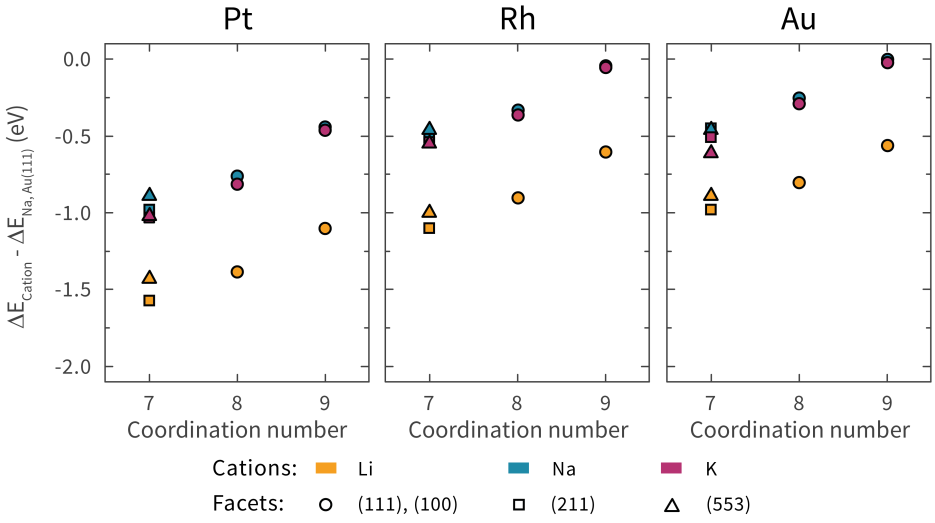

Fig. A.30 | Adsorption energies of Li, Na and K on various facets of Pt, Rh and Au, displayed as a function of the coordination number of the adsorption sites. Out of the flat surfaces, (111) has a coordination number of 9 and (100) has a coordination number of 8. Energies are normalized by subtracting the calculated adsorption energy of Na on Au(111), which is $-2\ eV$.

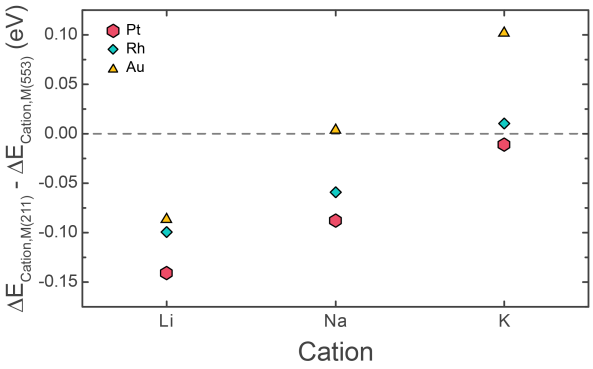

Fig. A.31 | Energy difference between adsorption on (211) and (553) facets. Lower values indicate a stronger preference for adsorption on the (211) facet. Positive values indicate a preference for adsorption to the (553) facet.

A.8 Coverage effects in cation adsorption

As mentioned in Chapter 4, opposite trends are found for cation adsorption on Pt steps and terraces. This is caused by the cation coverage being different for steps and terraces in our calculations. While a high cation coverage is adsorbed along step edges (1/2 monolayer (ML) per step atom), the stepped surfaces contain relatively wide terraces that lower the coverage per unit area compared to the low-index surfaces (1/3 monolayer on Pt(111) and 1/4 monolayer on Pt(100)). We found this coverage difference to be highly relevant to the trend in adsorption strength in our previous work:[3] the adsorption strength increased alongside cation size for low coverages, but showed the exact opposite behavior at high coverages. This is due to repulsive interactions between the cations being proportional to cation size: bigger cations interact more at high coverage due to their size, and also appear to retain more of their charge upon adsorbing. Large cations therefore experience both stronger steric and coulombic repulsion at high coverages, such that the adsorption trend reverses at coverages above 1/3 to 1/2 ML. The strong coverage dependence may also explain why adsorption appears weaker on some of the stepped surfaces than on the low-index surfaces, while we found the opposite to be true for 1/3 ML coverages on Pt step edges in our previous work.[4]

A.9 Potentials of zero surface energy

The curves in Fig. 4.10 in Chapter 4 cross zero at various potentials. These potentials are given in Table A.1. As can be seen in the table and Fig. 4.10, the potentials match relatively well with the experimental onset potentials and reproduce the similarity in onset potential between Pt and Rh, as well as Au having a significantly more negative onset potential.

Table A.1 | Fit values for spectra at various potentials.

Metal	**Facet**	**Hydrogen coverage**	**Potential of zero surface energy (V *vs.* RHE)**
Pt	(111)	1	-0.46
Pt	(100)	1	-0.45
Pt	(100)	1.25	-0.37
Rh	(111)	1	-0.53
Rh	(100)	1	-0.64
Rh	(100)	1.25	-0.47
Au	(111)	1	-0.72
Au	(100)	1	-0.66

A.10 Corrosion time effect on platinum

Fig. A.32 illustrates the effect of corrosion time on the final state of a platinum electrode. This effect is explored for an applied potential of -0.5 and -1.0 V *vs.* RHE and corrosion times between 1 and 10 minutes. For -0.5 V *vs.* RHE, a minor decrease in the (110) peak is seen when increasing the corrosion time from 1 to 5 minutes, while the surface remains similar when further extending the corrosion time to 10 minutes. For -1.0 V *vs.* RHE, no differences are seen when increasing the corrosion time from 1 to 10 minutes. SEM evaluation of the electrodes (not shown here) corroborates these findings.

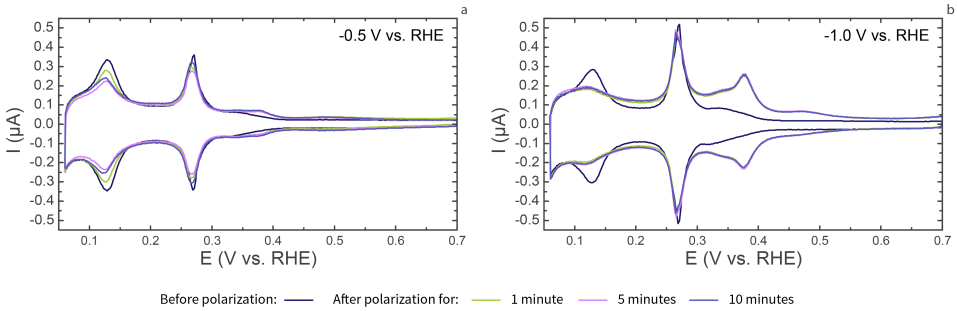

Fig. A.32 | CVs of platinum electrodes before (dark blue trace) and after cathodic polarization in 5 *M* NaOH at −0.5 *V vs.* RHE **(a)** and −1.0 *V vs.* RHE **(b)** for 1, 5 and 10 minutes. CV electrolyte: 0.5 *M* H_2SO_4. Scan rate: 50 $mV \cdot s^{-1}$.

References

1. Jeyabharathi, C., Ahrens, P., Hasse, U. & Scholz, F. Identification of low-index crystal planes of polycrystalline gold on the basis of electrochemical oxide layer formation. *Journal of Solid State Electrochemistry* **20,** 3025–3031 (2016).
2. Trasatti, S. & Petrii, O. Real surface area measurements in electrochemistry. *Pure and applied chemistry* **63,** 711–734 (1991).
3. McCrum, I. T. & Janik, M. J. Unpublished results.
4. McCrum, I. T. & Janik, M. J. First Principles Simulations of Cyclic Voltammograms on Stepped Pt(553) and Pt(533) Electrode Surfaces. *ChemElectroChem* **3,** 1609–1617 (2016).

B Supplementary Information for Chapter 5

B.1 *Operando* electrochemical flow cell

Fig. B.1 & B.2 display schematic drawings of the flow cell used in this study. The cell was mounted onto its aluminum holder (shown in Fig. 5.1) with two holes that fit around two pins on the holder. The bottom of the cell was covered with a 0.1 mm-thick fluorinated ethylene propylene (FEP) film and thin Kapton foil, which were held in place by an aluminum cover plate. With the FEP film pressed against the polyether ether ketone (PEEK) body of the cell, a thin channel was formed. This channel facilitated the flow of the electrolyte, which was fed in and drained from holes in the side of the cell.

Within the flow cell channel, a Pt strip was used as the counter electrode and placed alongside the working electrode. This strip was made from a $\varnothing = 0.8\ mm$ Pt wire (Mateck, 99.9%), of which one end was bent and flattened in a rolling press. The bent electrode was sealed into the cell with a custom-made Teflon ferrule and a hollow PEEK connector. The flow channel also contained the HydroFlex working electrode, which was sealed with a Viton O-ring.

Finally, the flow channel contained the $\varnothing = 3\ mm$ gold disk electrode. This disk was held in place by a Teflon sheath, as can be seen in the Section view in Fig. B.2. Electrical contact with the reference electrode was established by a spring contact, which screwed into the back of the sheath.

B.2 Additional X-ray absorption spectra

Fig. B.3 presents X-ray absorption spectra in a wider energy range than those in Fig. 5.2. Fig. B.3 shows good overlap between the spectra at higher energies. This indicates consistent normalization for all presented spectra. Additionally, this overlap indicates the overall structure of the nanoparticles to be maintained during the experiments.

Fig. B.4 compares the XANES spectra of Pt nanoparticles, measured at 0 and 0.4 V *vs.* RHE. Though the spectra overlap reasonably well, there is a small positive edge shift upon decreasing the electrode potential. This shift is accompanied by a minor whiteline intensity decrease and slight absorption increase at higher absorption energies. These changes were previously assigned to the adsorption of hydrogen on platinum.[1] This is in general agreement with the difference spectrum for 0 V *vs.* RHE in Fig. 5.3 **a**.

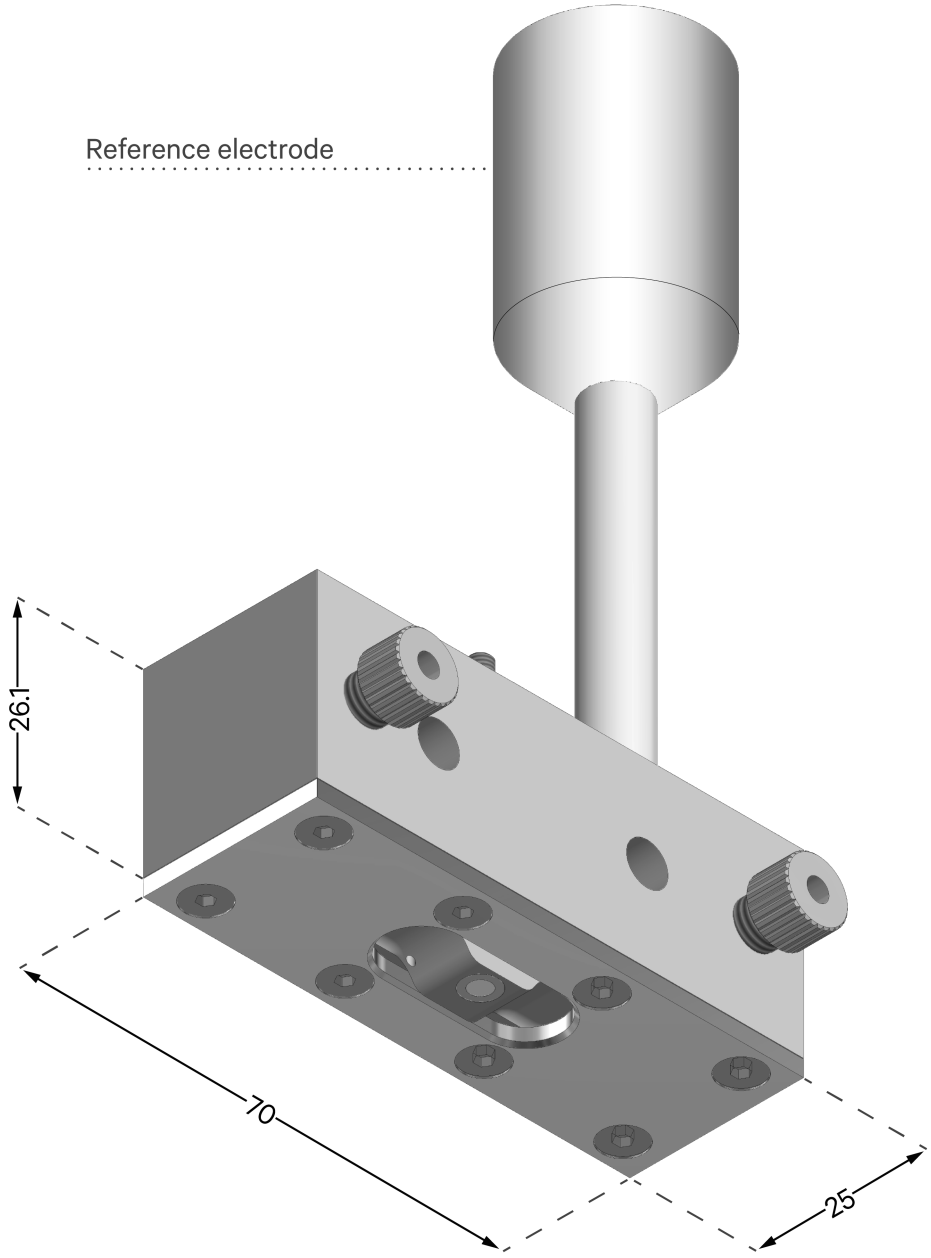

Fig. B.1 | Schematic overview of the employed flow cell. Sizes are in millimeters.

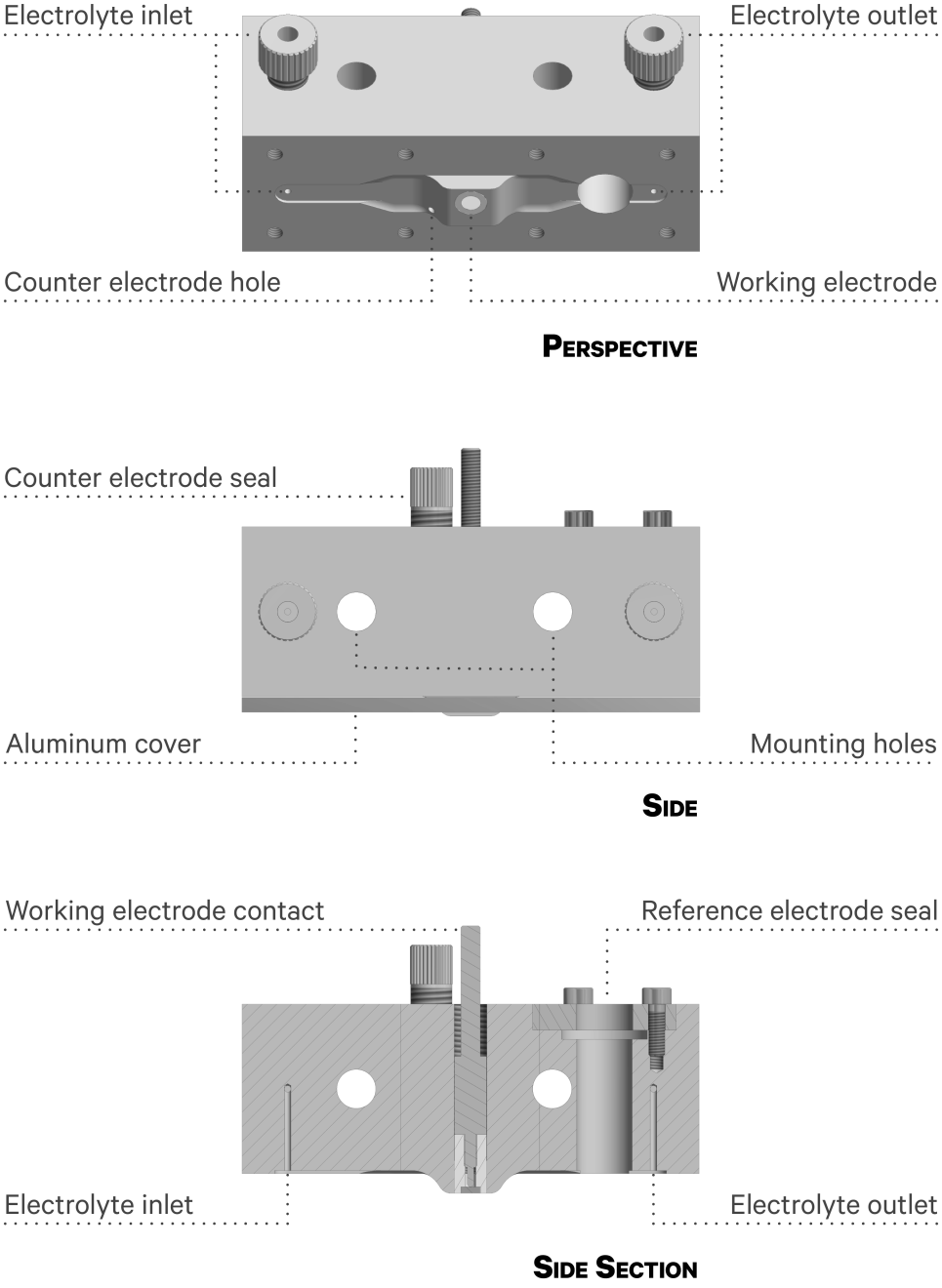

Fig. B.2 | Various schematic views of the employed flow cell. Aluminum cover plate is not shown in Perspective and Side Section.

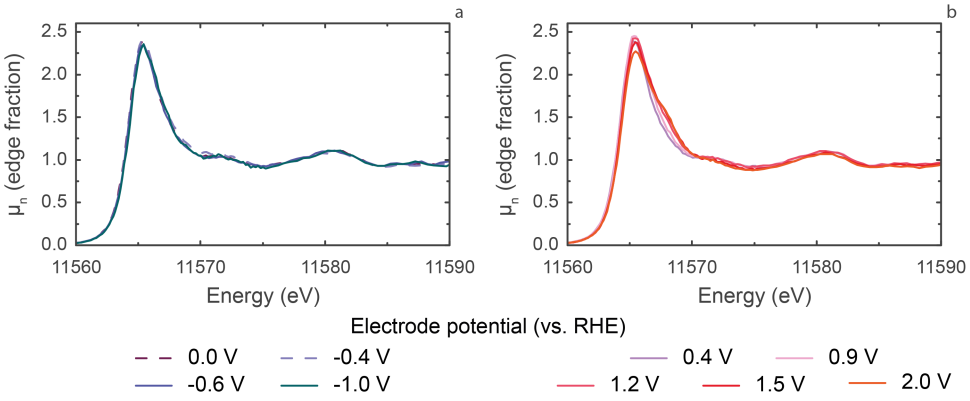

Fig. B.3 | Expanded view of the X-ray absorption spectra shown in Chapter 5. Spectra are given for cathodic potentials **(a)** and anodic potentials **(b)**

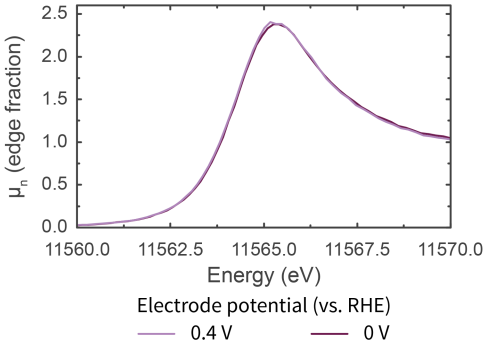

Fig. B.4 | Comparison of X-ray absorption spectra of Pt at 0 and 0.4 *V* *vs.* RHE.

B.3 Fit results

The peaks in Fig. 5.4 were fitted to the experimental spectra between 11560 *eV* and 11572 *eV*, using the peak fitting function in ATHENA.[2] To fit the spectra, three functional shapes were used.[1] First of all, an arctangent was used to account for the background. This arctangent was centered at 11564 *eV* and had a fixed width of 0.5 *eV*. Secondly, a pseudo-Voigt peak was used to fit the whiteline. This peak will be referred to as the "low-energy peak". It was centered at 11565.4 *eV* and the Gaussian/Lorentzian mixing ratio was fixed to 0.5. The peak width and height were allowed to vary. Thirdly, an additional pseudo-Voigt peak was used to fit the whiteline shoulder. This peak will be referred to

as the "high-energy peak". It was centered at $11567.55\ eV$ and the Gaussian/Lorentzian mixing ratio was fixed to 0.5. The peak width and height were allowed to vary. In ATHENA, the pseudo-Voigt peaks are normalized, such that their height equals their area. Representative fits are given in Fig. B.5, whereas the fit results for all data points are shown in Table B.1.

Table B.1 | Fit values for spectra at various potentials. Potentials are given *vs.* RHE

Applied potential	**Background**	**Low-energy peak**		**High-energy peak**		**R-factor**
	A_{bg}	A_2	ΔE_1	A_2	ΔE_2	
2.0 V	0.97 ± 0.01	3.81 ± 0.05	2.36 ± 0.03	1.83 ± 0.09	2.8 ± 0.1	0.000646
1.8 V	0.97 ± 0.01	3.83 ± 0.05	2.32 ± 0.03	1.9 ± 0.1	2.8 ± 0.1	0.000668
1.5 V	0.98 ± 0.01	4.09 ± 0.05	2.35 ± 0.03	1.8 ± 0.1	2.8 ± 0.1	0.000611
1.2 V	1.00 ± 0.01	4.28 ± 0.05	2.34 ± 0.03	1.42 ± 0.08	2.6 ± 0.1	0.000593
0.9 V	1.018 ± 0.009	4.87 ± 0.05	2.53 ± 0.03	0.67 ± 0.07	2.1 ± 0.2	0.000647
0.4 V	1.023 ± 0.009	4.93 ± 0.06	2.63 ± 0.04	0.27 ± 0.06	1.4 ± 0.3	0.000953
0 V	1.042 ± 0.009	4.71 ± 0.06	2.58 ± 0.03	0.33 ± 0.05	1.6 ± 0.2	0.000816
-0.2 V	1.044 ± 0.009	4.85 ± 0.06	2.58 ± 0.04	0.43 ± 0.06	1.8 ± 0.2	0.000860
-0.4 V	1.07 ± 0.01	4.52 ± 0.06	2.51 ± 0.03	0.53 ± 0.07	2.0 ± 0.2	0.000723
-0.6 V	1.023 ± 0.008	4.49 ± 0.05	2.51 ± 0.03	0.50 ± 0.06	2.0 ± 0.2	0.000669
-0.7 V	1.007 ± 0.009	4.34 ± 0.05	2.49 ± 0.03	0.50 ± 0.06	1.9 ± 0.2	0.000767
-0.8 V	1.032 ± 0.009	4.28 ± 0.05	2.38 ± 0.03	0.77 ± 0.07	2.1 ± 0.2	0.000736
-0.9 V	1.050 0.009	4.10 ± 0.05	2.37 ± 0.03	0.65 ± 0.08	2.4 ± 0.3	0.000686
-1.0 V	1.01 ± 0.01	4.21 ± 0.06	2.43 ± 0.04	0.81 ± 0.09	2.4 ± 0.2	0.000934

Table B.1 gives the fit results that were used to make Fig. 5.4. The table contains the following variables: A_{bg} is the step height of the background arctangent; A_1 is the height of the low-energy peak; ΔE_1 is the half width at half maximum (HWHM) of the low-energy peak; A_2 is the height of the high-energy peak; and ΔE_2 is the HWHM of the high-energy peak. This notation is chosen to be consistent with previous work from literature.[1] Note, however, that this previous work used unnormalized pseudo-Voigt functions.

All fit results in Table B.1 are given with an error. This error equals the standard deviation, as given in the fit results from ATHENA. The only value without an associated error is the R-factor. This factor quantifies the mismatch between the fit and the data and is also taken from the ATHENA fit results. The value for the R-factor is given by equation B.1.[3]

$$R = \frac{\sum_{i=1}^{N}(data_i - fit_i)^2}{\sum_{i=1}^{N}(data_i)^2} \tag{B.1}$$

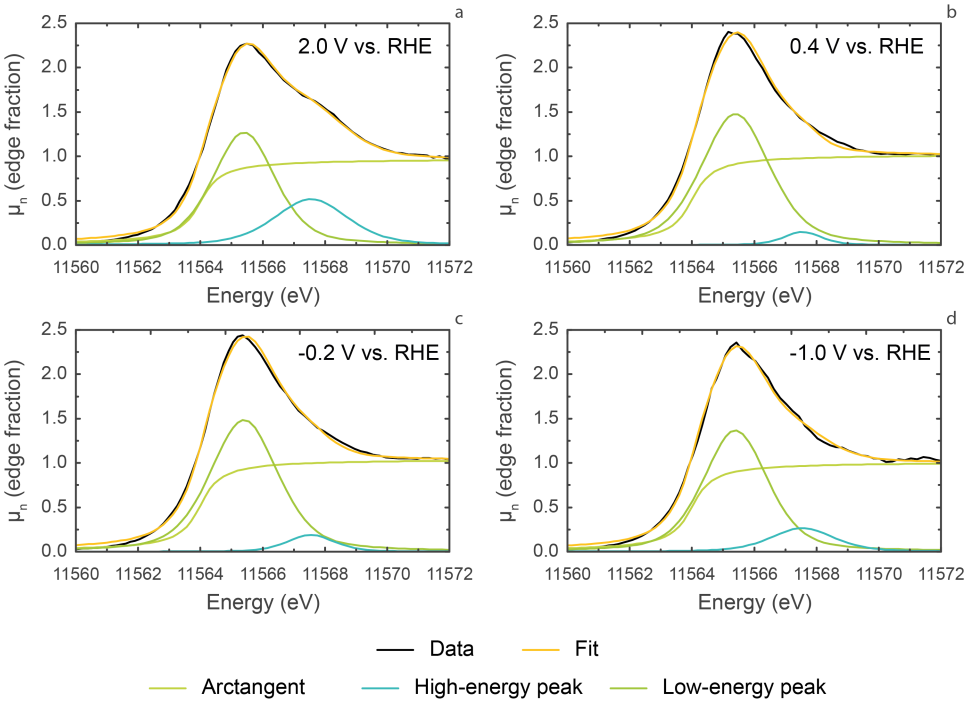

Fig. B.5 | Representative fits of X-ray absorption spectra of electrodes polarized at 2.0 *V vs.* RHE **(a)**, 0.4 *V vs.* RHE **(b)**, −0.2 *V vs.* RHE **c** and −1.0 *V vs.* RHE.

Here, an R-factor closer to zero equals a better fit.

Representative fits are displayed in Fig. B.5 for four representative potentials. This figure confirms the quality of the fit that is indicated by the low R-factor values in Table B.1.

B.4 Expanded modeled spectra

Fig. B.6 shows the spectra modeled with OCEAN, over a wider energy range than Fig. 5.5. From Fig. B.6, it appears that the modeled spectra overestimate some of the spectral features. This is most readily seen by comparing the white line intensity around 11565 *eV* with the experimental whiteline intensity; the modeled intensity is approximately 1.5 times higher than in experiments. Similar, though less pronounced, deviations are found for the smaller peaks. However, the location of these peaks and shoulders agrees rather well with those in experimental spectra.

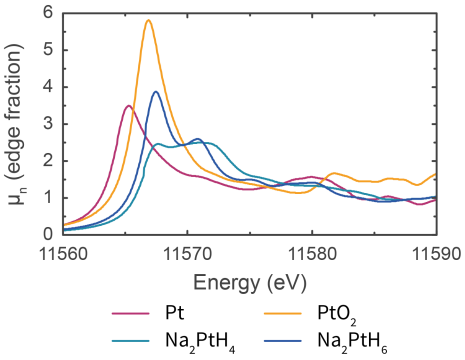

Fig. B.6 | Expanded view of the modeled X-ray absorption spectra shown in Chapter 5.

References

1. Merte, L. R. *et al.* Electrochemical Oxidation of Size-Selected Pt Nanoparticles Studied Using in Situ High-Energy-Resolution X-ray Absorption Spectroscopy. *ACS Catalysis* **2,** 2371–2376 (2012).
2. Ravel, B. & Newville, M. ATHENA , ARTEMIS , HEPHAESTUS: data analysis for X-ray absorption spectroscopy using IFEFFIT. *Journal of Synchrotron Radiation* **12,** 537–541 (2005).
3. Calvin, S. *XAFS for Everyone* 1st ed. **1,** 427 (CRC Press, Boca Raton, FL, 2013).

C Supplementary Information for Chapter 6

C.1 Electrodes employed in this study

Fig. C.1 displays normalized blank cyclic voltammograms (CVs) of the electrodes used in the current study. The shape of these voltammograms is in good agreement with literature voltammograms of corresponding single- and polycrystalline Pt electrodes.[1,2] The voltammograms were normalized using the integrated anodic current densities, without correcting for the double layer.[1,2]

All ORR current densities in this article are reported by normalizing with respect to the *geometric* electrode surface area, as is appropriate when considering reactant mass transport through diffusion or convection.[3] The geometric surface areas of most of the employed electrodes differed by no more than 2% from the electrochemically calculated surface area. The only exception to this statement is Pt(111), for which the electrochemical surface area was 13% smaller than the geometric surface area. Similar deviations were obtained for a different Pt(111) crystal. For Pt(111), normalizing currents by the geometric surface area was therefore critical in calculating limiting current densities that match the Levich equation.

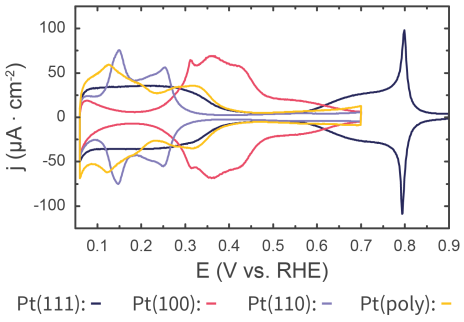

Fig. C.1 | Cyclic voltammograms of the employed electrodes: Pt(111), Pt(100), Pt(110) and Pt(poly). Voltammograms were recorded in 0.1 M $HClO_4$, at a scan rate of 50 $mV \cdot s^{-1}$.

C.2 Comparison of Pt(111) electrodes after cathodic corrosion

Fig. C.2 shows CVs of Pt(111) after cathodic corrosion at various potentials in 1 M NaOH. As can be seen in the figure, there are no significant differences in the post-corrosion voltammograms, as function of the corrosion potential.

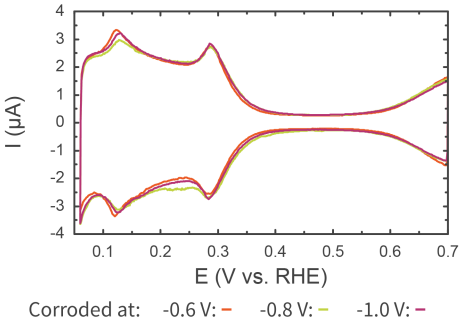

Fig. C.2 | Cyclic voltammograms of Pt(111) after cathodic corrosion at various potentials in 1 M NaOH. Voltammograms were recorded in 0.1 M $HClO_4$, at a scan rate of 50 $mV \cdot s^{-1}$.

C.3 Validation of the HMRD setup

Fig. C.3 displays cyclic voltammograms for the ORR activity of Pt(111). The CVs contain no pronounced oscillations, which indicates proper concentric alignment of the single crystal. Furthermore, the voltammograms at 0, 200, 400 and 900 rpm contain the characteristic 'butterfly' feature around 0.8 V *vs.* RHE. The presence of the butterfly and the decrease of its intensity with increasing rotation rate is a strong sign of electrolyte cleanliness.[4,5]

Fig. C.4 shows Levich plots for each of the electrodes in this study. The theoretical Levich plots were calculated using the Levich equation:[6]

$$j_L = 0.62 \cdot n \cdot F \cdot D_{O_2}^{\frac{2}{3}} \cdot \omega^{\frac{1}{2}} \cdot \nu^{-\frac{1}{6}} \cdot C_{O_2}^{*} \tag{C.1}$$

Here, n equals the amount of transferred electrons; F equals Faraday's constant; D_{O_2} equals the oxygen diffusion constant, ω equals the radial electrode rotation rate; ν equals the kinematic viscosity of the solution; and $C_{O_2}^{*}$ equals the oxygen concentration. For the studied system, the parameters take the following values: $n = 4$ for the conversion from

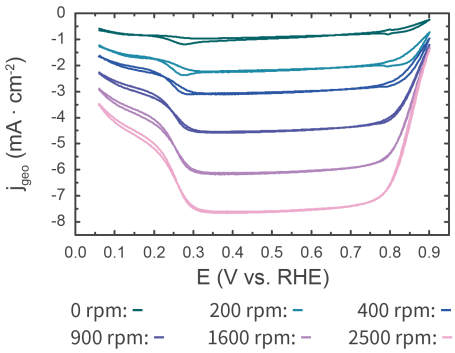

Fig. C.3 | Cyclic voltammograms for oxygen reduction on Pt(111), at various rotation rates. Voltammograms were recorded in oxygen-saturated 0.1 M $HClO_4$, at a scan rate of 50 $mV \cdot s^{-1}$.

O_2 to H_2O; $D_{O_2} = 1.384\ mM$;[7] $\nu = 8.93 \cdot 10^{-3}\ cm^2 \cdot s^{-1}$;[8] and $C^*_{O_2} = 1.67 \cdot 10^{-5}\ cm^2 \cdot s^{-1}$.[7]

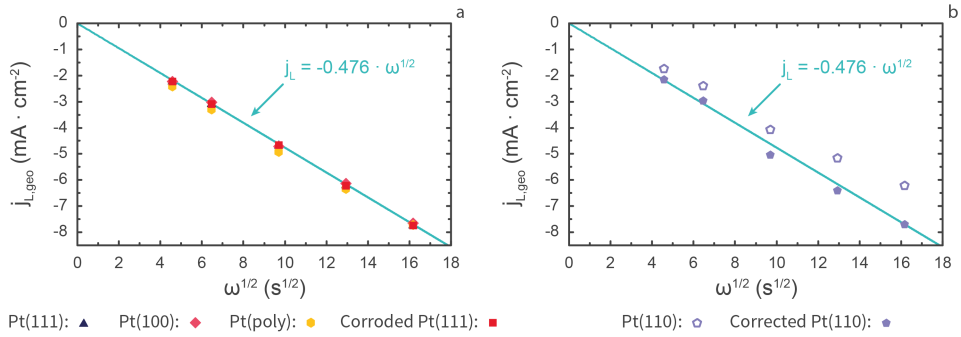

Fig. C.4 | Levich plots for the ORR on Pt(111), Pt(100), Pt(poly) and Pt(111) which was corroded at −1.0 V *vs.* RHE in 1 M NaOH **(a)**. Corrected and uncorrected Levich plots for the ORR on Pt(110) **(b)**. Voltammograms for acquiring the plotted datapoints were recorded in 0.1 M $HClO_4$, at a scan rate of 50 $mV \cdot s^{-1}$.

As can be seen in Fig. C.4 **a**, the Pt(111), Pt(100), Pt(poly) and corroded Pt(111) electrodes are described well by the theoretical Levich plot. However, Fig. C.4 **b** demonstrates that the theoretical behavior is matched less well by Pt(110), for which 20% *lower* Levich slope is obtained. This change in slope is not due to wetting of the side of the electrode, which should increase the magnitude of the slope.[9] The slope change is also not related to dynamic changing of the meniscus shape during rotation, which should cause

a vertical offset in the Levich plot.[9]

Instead, the slope change must be ascribed to a decrease in the apparent electrode area. This is demonstrated by 'correcting' the current densities by dividing them by the relative difference between the obtained current density and the theoretical current density at 2500 rpm. This corrected curve is represented by the filled pentagons in Fig. C.4 **b** and matches the theoretical Levich plot well. The deviations from ideal diffusion behavior are therefore compensated for when normalizing the data as done in Fig. 6.3.

C.4 Kinetic ORR current densities

The ORR activity of the electrodes can also be assessed by calculating kinetic current densities at 0.9 V *vs.* RHE. These kinetic current densities are calculated by rewriting the Levich equation to:[10]

$$\frac{1}{j} = \frac{1}{j_k} + B \cdot \omega^{-\frac{1}{2}} \tag{C.2}$$

Here, j_k is the kinetic current density and B depends on the various parameters in the Levich equation. j_k is obtained from equation C.2 by plotting the inverse current density *versus* $\omega^{-\frac{1}{2}}$ in a Koutecky-Levich plot. From such a plot, the intercept is obtained through a linear least-squares fit and j_k is then obtained as the inverse of the intercept. The result of this procedure is plotted for all studied electrodes in Fig. C.5.

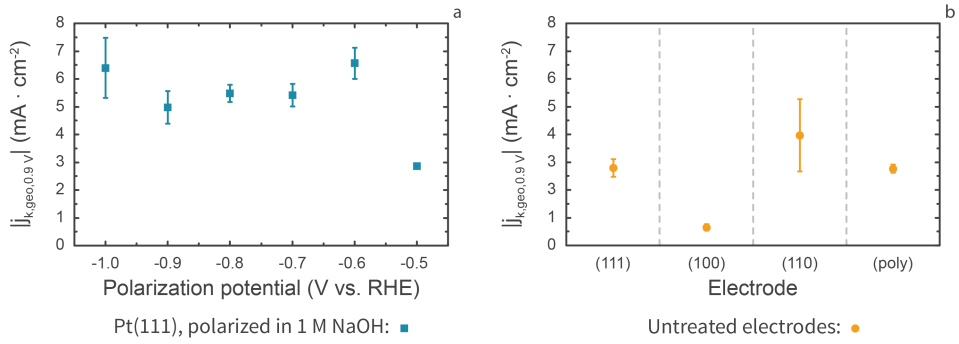

Fig. C.5 | Kinetic ORR current densities of corroded Pt(111) (red squares), as function of the polarization potential **(a)** and of uncorroded electrodes (yellow circles) **(b)**. Rotation rate: 1600 rpm. Each data point is the average of 3 or more experiments. Error bars represent one standard deviation.

As can be seen, Fig. C.5 is in good qualitative agreement with Fig. 6.3. The slightly larger error bars in Fig. C.5 are related to slight variations in the recorded current densities due to small variations in the meniscus height. Finally, it should be noted that the kinetic current density for Pt(110) in Fig. C.5 is *not corrected* for the aforementioned reduced surface area and is therefore underestimated.

C.5 Pt(111), corroded in 10 M NaOH

Fig. C.6 displays CVs of Pt(111), corroded at and slightly below the onset potential in 10 *M* NaOH. These experiments were explorative in nature and were therefore only performed once, with a different Pt(111) electrode.

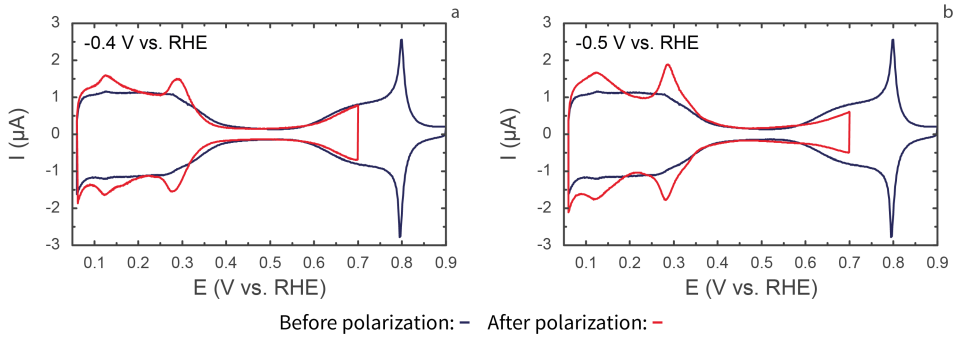

Fig. C.6 | Cyclic voltammograms of Pt(111) before (blue trace) and after (red trace) cathodic polarization in 10 *M* NaOH at −0.4 *V vs.* RHE **(a)** and −0.5 *V vs.* RHE **(b)**. Voltammograms were recorded in 0.1 *M* $HClO_4$, at a scan rate of 50 $mV \cdot s^{-1}$.

The electrode in Fig. C.6 **a** appears similar to those in Fig. 6.1 and Fig. C.2, with an approximately 15% apparent area increase. Indeed, the normalized ORR activity of this electrode at 0.9 *V vs.* RHE and 1600 *rpm* is similar to those in Chapter 6: 0.32. In contrast, Fig. C.6 **b** indicates significantly more (110) and (100) step sites after corrosion at −0.5 *V vs.* RHE and a roughly 25% area increase. Interestingly, the electrode has a *lower* normalized ORR activity of 0.27. In fact, the normalized ORR activity in these explorative experiments decreased monotonically with more negative corrosion potentials. The lowest normalized activity of 0.2 was reached at the most negative explored potential of −0.8 *V vs.* RHE.

References

1. Gomez, R., Orts, J. M., Alvarez-Ruiz, B. & Feliu, J. M. Effect of Temperature on Hydrogen Adsorption on Pt(111), Pt(110), and Pt(100) Electrodes in 0.1 M $HClO_4$. *The Journal of Physical Chemistry B* **108,** 228–238 (2004).
2. Chen, Q.-S., Solla-Gullón, J., Sun, S.-G. & Feliu, J. M. The potential of zero total charge of Pt nanoparticles and polycrystalline electrodes with different surface structure: The role of anion adsorption in fundamental electrocatalysis. *Electrochimica Acta* **55,** 7982–7994 (2010).
3. Bard, A. J. & Faulkner, L. R. in *Electrochemical Methods: Fundamentals and Applications* 2nd ed. Chap. 5 (Wiley, New York, 2001).
4. Gómez-Marín, A. M., Rizo, R. & Feliu, J. M. Some reflections on the understanding of the oxygen reduction reaction at Pt(111). *Beilstein Journal of Nanotechnology* **4,** 956–967 (2013).
5. Gómez-Marín, A. M., Rizo, R. & Feliu, J. M. Oxygen reduction reaction at Pt single crystals: a critical overview. *Catalysis Science & Technology* **4,** 1685 (2014).
6. Bard, A. J. & Faulkner, L. R. in *Electrochemical Methods: Fundamentals and Applications* 2nd ed. Chap. 9 (Wiley, New York, 2001).
7. Wakabayashi, N., Takeichi, M., Itagaki, M., Uchida, H. & Watanabe, M. Temperature-dependence of oxygen reduction activity at a platinum electrode in an acidic electrolyte solution investigated with a channel flow double electrode. *Journal of Electroanalytical Chemistry* **574,** 339–346 (2005).
8. Wang, W. *et al.* Carbon-supported Pd-Co bimetallic nanoparticles as electrocatalysts for the oxygen reduction reaction. *Journal of Power Sources* **167,** 243–249 (2007).
9. Villullas, H. & Teijelo, M. The hanging-meniscus rotating disk (HMRD) Part 1. Dependence of hydrodynamic behavior on experimental variables. *Journal of Electroanalytical Chemistry* **384,** 25–30 (1995).
10. Schmickler, W. & Santos, E. in *Interfacial Electrochemistry* 2nd ed. Chap. 20 (Springer Berlin, Heidelberg, 2010).

D Supplementary Information for Chapter 7

D.1 EXAFS functions in R-space

Fig. D.1 displays the EXAFS functions in R-space for the alloy particles studied in Chapter 7. Though these graphs display an intensity as function of R, one should note that the graphs are not radial distribution functions.[1]

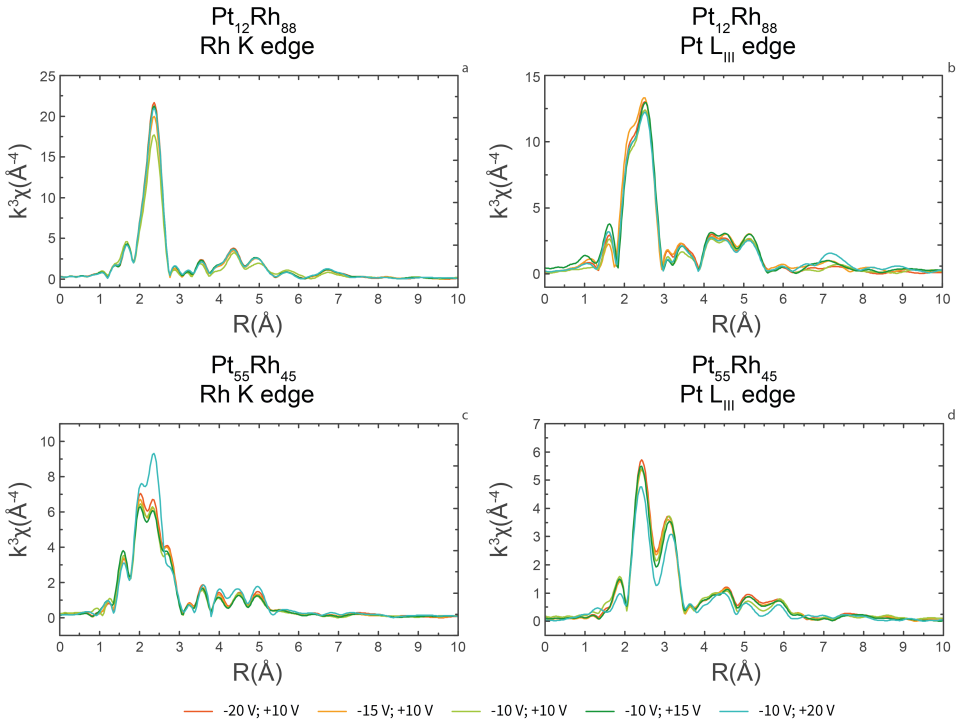

Fig. D.1 | EXAFS functions in R-space for the Rh K edge of $Pt_{12}Rh_{88}$ particles **(a)**, the Pt L_{III} edge of $Pt_{12}Rh_{88}$ particles **(b)**, the Rh K edge of $Pt_{55}Rh_{45}$ particles **(c)** and the Pt L_{III} edge of $Pt_{55}Rh_{45}$ particles **(d)**, prepared at various potentials.

D.2 Nanoparticle X-ray diffraction patterns

Fig. D.2 displays X-ray diffraction patterns of all studied nanoparticles. Several peaks in the diffraction pattern do not correspond to the nanoparticles. Instead, they correspond to reflections of the boron nitride matrix in which the particles were embedded. These peaks are indicated with a blue circle.

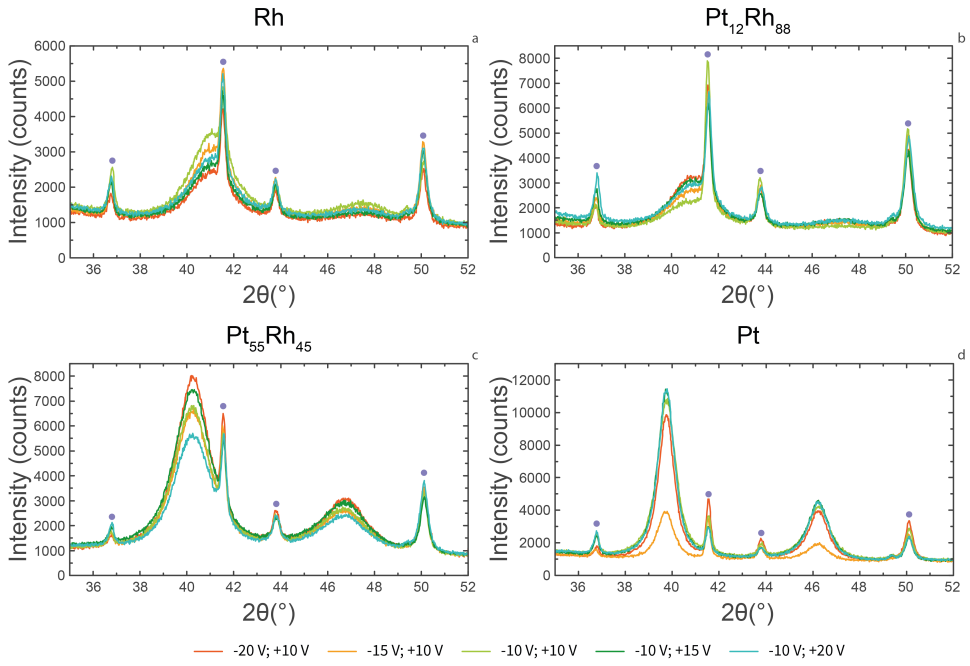

Fig. D.2 | X-ray diffraction patterns of Rh **(a)**, $Pt_{12}Rh_{88}$ **(b)**, $Pt_{55}Rh_{45}$ **(c)** and Pt **(d)** particles, prepared at various potentials. Peaks marked with a circle correspond to boron nitride reflections.

D.3 Particle sizes as determined by transmission electron microscopy

Transmission electron microscopy (TEM) samples were prepared by mixing a droplet of nanoparticle suspension with $1.5\ mL$ of ethanol (Sigma-Aldrich, puriss. p.a.). This mixture was then applied on a TEM grid (Formvar film on copper 300 mesh) and subsequently air-dried. All TEM data were obtained using a JEOL TEM 1010. Average particle sizes and size standard deviations, given in Table D.1, were calculated by analyzing 200 particles per sample. Particle size distributions for Rh, $Pt_{12}Rh_{88}$, $Pt_{55}Rh_{45}$ and Pt were generated by analyzing the same 200 particles per sample. These distributions are displayed in Fig. D.3, Fig. D.4, Fig. D.5, and Fig. D.6, respectively. If agglomerated particles were present, these particles were not treated as one large particle. Rather, the individual primary crystallites were counted as individual particles, in order to facilitate a direct comparison with the X-ray diffraction-based coherent domain sizes.

Table D.1 | Average particle sizes and standard deviations for all alloys and potential limits. Particle sizes are given in nanometers

Potential Limits	**Rh**	**$Pt_{12}Rh_{88}$**	**$Pt_{55}Rh_{45}$**	**Pt**
-20 V; +10 V	2.5 ± 0.7	1.9 ± 0.4	3.9 ± 0.8	17 ± 6
-15 V; +10 V	2.2 ± 1.0	2.2 ± 0.7	2.8 ± 1.0	3.4 ± 2.1
-10 V; +10 V	1.3 ± 0.5	1.8 ± 0.7	3.0 ± 0.8	1.7 ± 0.5
-10 V; +15 V	2.3 ± 0.7	2.3 ± 0.5	2.7 ± 1.2	1.8 ± 0.7
-10 V; +20 V	1.0 ± 0.3	1.6 ± 0.7	2.3 ± 0.9	18 ± 6

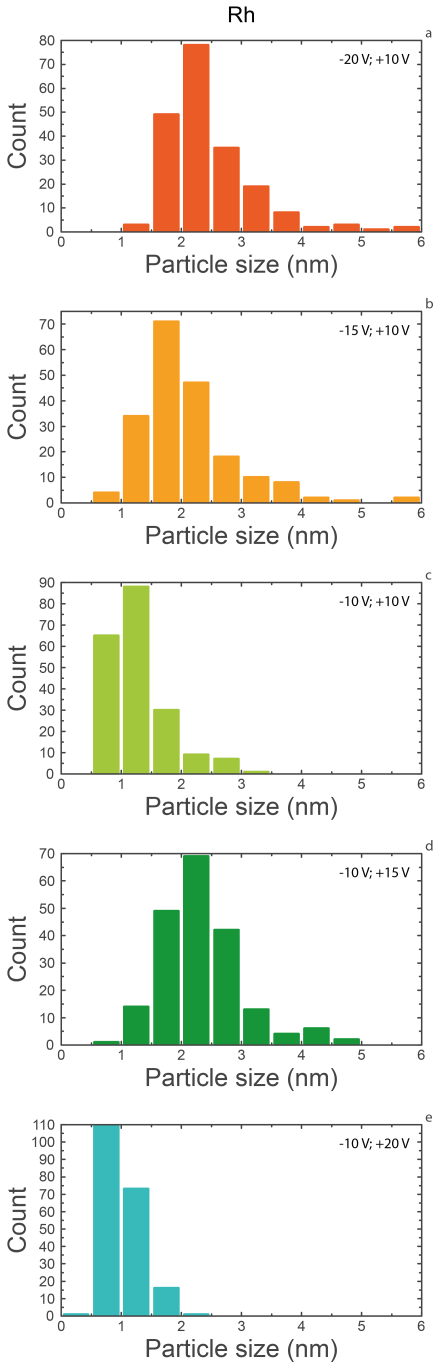

Fig. D.3 | Particle size distributions for studied Rh nanoparticles.

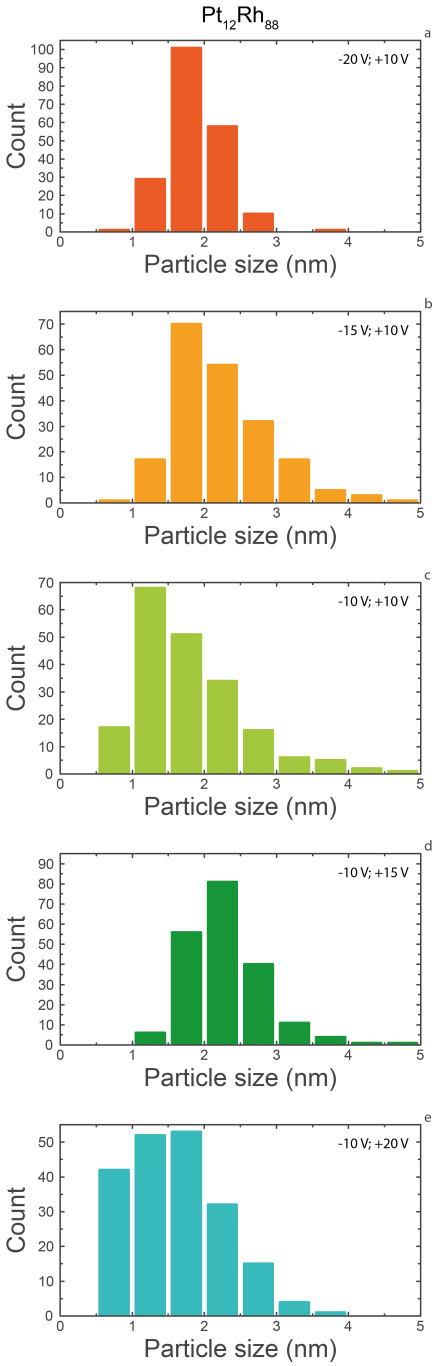

Fig. D.4 | Particle size distributions for studied $Pt_{12}Rh_{88}$ nanoparticles.

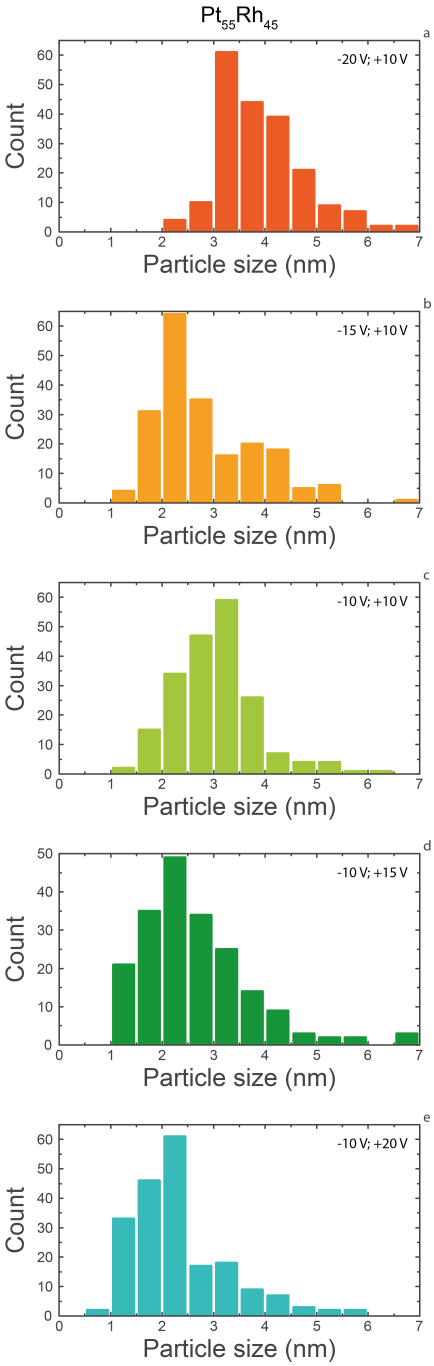

Fig. D.5 | Particle size distributions for studied $Pt_{55}Rh_{45}$ nanoparticles.

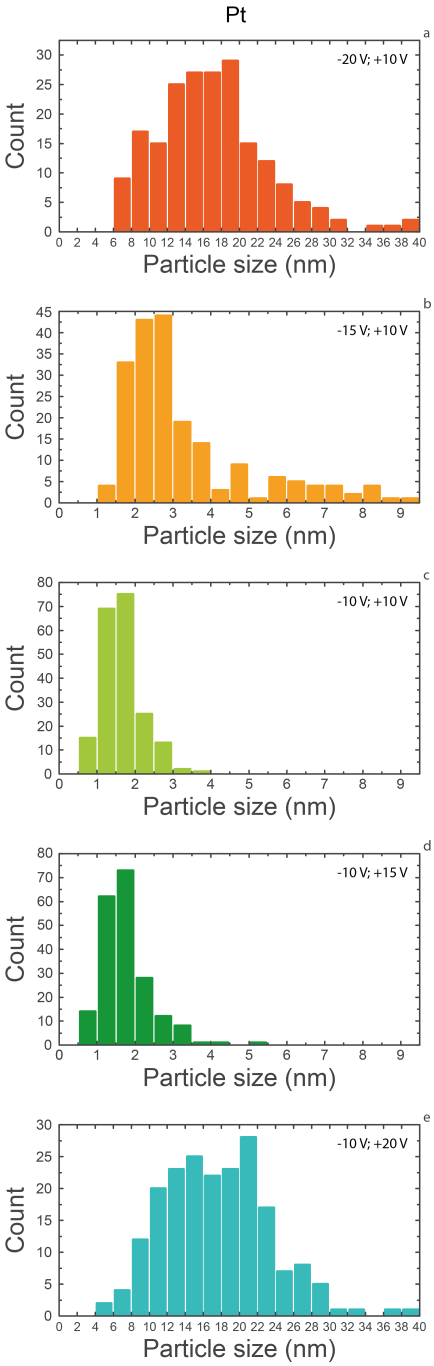

Fig. D.6 | Particle size distributions for studied Pt nanoparticles.

D.4 2D nanoparticle visualizations

This section provides 2D visualizations of the data presented in Fig. 7.4 of Chapter 7. These visualizations, shown in Fig. D.7, consist of one layer of rhodium and platinum atoms. As such, they approximate a 2D cut through a nanoparticle.

For each model, containing 100 atoms, one can estimate the local Pt content that would be observed for these models through Rh K edge and Pt L_{III} edge EXAFS experiments. This is done by counting the number of neighboring platinum atoms ($n_{Pt,i}$) for each atom i in the model and dividing by the total number of neighboring atoms ($n_{t,i}$) for that atom i. For each atom, this yields the local relative platinum content ($x_{Pt,i}$):

$$x_{Pt,i} = \frac{n_{Pt,i}}{n_{t,i}} \cdot 100\% \tag{D.1}$$

Averaging this value over either all platinum or all rhodium atoms will lead to an approximation of the Pt edge- and Rh edge-based platinum content, respectively.

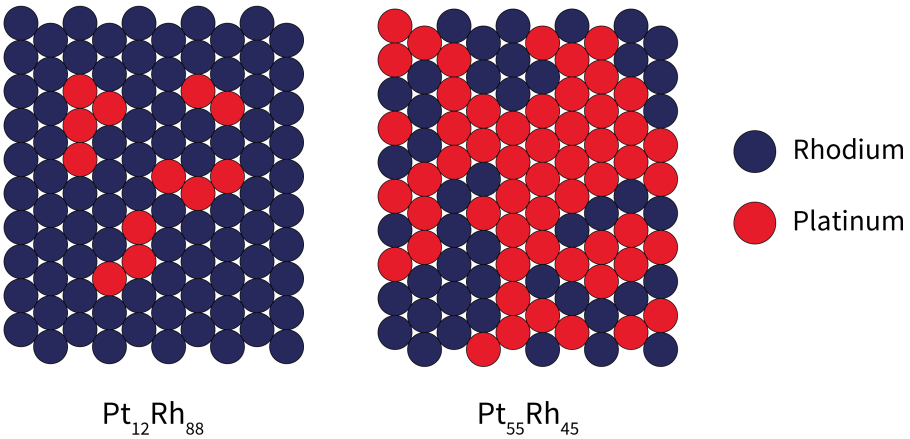

Fig. D.7 | 2D visualizations of the studied $Pt_{12}Rh_{88}$ and $Pt_{55}Rh_{45}$ nanoparticles.

The $Pt_{12}Rh_{88}$ surface in Fig. D.7 gives a Pt edge-based platinum content of 25.0% and a Rh edge-based platinum content of 10.2%. In the $Pt_{55}Rh_{45}$ example, the Pt edge-based platinum content is 61.3% and the Rh edge-based platinum content is 51.2%. Though these numbers agree relatively well with the actual data, care should be taken when extrapolating these models as accurate reflections of 3-dimensional nanoparticles. Nonetheless, the two examples can be taken as reasonable first-order approximations of the average elemental distribution of the studied nanoparticles.

References

1. Calvin, S. *XAFS for Everyone* 1st ed. **1,** 427 (CRC Press, Boca Raton, FL, 2013).